



Deposited via The University of Sheffield.

White Rose Research Online URL for this paper:

<https://eprints.whiterose.ac.uk/id/eprint/117580/>

Version: Accepted Version

---

**Article:**

Lewis, C.J., Sancho, C., McDonald, E.V. et al. (2017) Post-tectonic landscape evolution in NE Iberia using staircase terraces: Combined effects of uplift and climate. *Geomorphology*, 292. pp. 85-103. ISSN: 0169-555X

<https://doi.org/10.1016/j.geomorph.2017.04.037>

---

Article available under the terms of the CC-BY-NC-ND licence  
(<https://creativecommons.org/licenses/by-nc-nd/4.0/>)

**Reuse**

Items deposited in White Rose Research Online are protected by copyright, with all rights reserved unless indicated otherwise. They may be downloaded and/or printed for private study, or other acts as permitted by national copyright laws. The publisher or other rights holders may allow further reproduction and re-use of the full text version. This is indicated by the licence information on the White Rose Research Online record for the item.

**Takedown**

If you consider content in White Rose Research Online to be in breach of UK law, please notify us by emailing [eprints@whiterose.ac.uk](mailto:eprints@whiterose.ac.uk) including the URL of the record and the reason for the withdrawal request.

1  
2  
3  
4 1 **Post-tectonic landscape evolution in NE Iberia using staircase terraces:**  
5  
6 2 **combined effects of uplift and climate**  
7  
8

9  
10 3 Claudia J. Lewis<sup>1</sup>, Carlos Sancho<sup>2\*</sup>, Eric V. McDonald<sup>3</sup>, José Luis Peña-Monné<sup>4</sup>, Emilio L.  
11  
12 4 Pueyo<sup>5,6</sup>, Edward Rhodes<sup>7</sup>, Mikel Calle<sup>8</sup>, Ruth Soto<sup>5,6</sup>  
13  
14

15 5 <sup>1</sup> Earth and Environmental Sciences Division, Los Alamos National Laboratory, 87545  
16  
17 6 Los Alamos, NM, USA  
18  
19

20  
21 7 <sup>2</sup> Ciencias de la Tierra, Universidad de Zaragoza, Pedro Cerbuna 12, 50009 Zaragoza,  
22  
23 8 Spain  
24  
25

26 9 <sup>3</sup> Desert Research Institute, 2215 Raggio Parkway, Reno, NV, USA  
27  
28  
29

30 10 <sup>4</sup> Geografía y Ordenación del Territorio, Universidad de Zaragoza, Pedro Cerbuna 12,  
31  
32 11 50009 Zaragoza, Spain  
33  
34

35 12 <sup>5</sup> Instituto Geológico y Minero de España, Unidad de Zaragoza, Manuel Lasala 44,  
36  
37 13 50006 Zaragoza, Spain  
38  
39

40  
41 14 <sup>6</sup> Unidad Asociada en Ciencias de la Tierra IGME-Universidad de Zaragoza  
42  
43

44 15 <sup>7</sup> Department of Geography, The University of Sheffield, Sheffield S10 2TN, UK  
45  
46

47 16 <sup>8</sup> Museo Nacional de Ciencias Naturales, CSIC, José Gutiérrez Abascal 2, 28006 Madrid,  
48  
49 17 Spain  
50

51  
52  
53 18 **\* Corresponding author:**  
54  
55  
56  
57  
58  
59

60  
61  
62 19 Carlos Sancho Marcén  
63  
64 20 Departamento de Ciencias de la Tierra  
65  
66  
67 21 Universidad de Zaragoza  
68  
69 22 Pedro Cerbuna, 12  
70  
71 23 50009 Zaragoza  
72  
73 24 Spain  
74  
75  
76 25 Email: csancho@unizar.es  
77  
78 26 Phone: +34976761091  
79  
80  
81 27  
82  
83  
84  
85 28  
86  
87  
88 29  
89  
90  
91 30  
92  
93  
94  
95 31  
96  
97  
98 32  
99  
100  
101 33  
102  
103  
104  
105 34  
106  
107  
108 35  
109  
110  
111 36  
112  
113  
114  
115 37  
116  
117  
118

**Abstract**

River incision into bedrock resulting from the combined effects of tectonic uplift and climate governs long-term regional landscape evolution. We determined spatial and temporal patterns of post-orogenic stream incision from a sequence of well-preserved staircase terraces developed over the last 1 Ma in the Central Pyrenees and its southern foreland Ebro basin (NE Spain). Extensive remnants of ten vertically separated terraces (Qt1 to Qt10, from oldest to youngest) were mapped along 170 km of the Cinca River valley, transverse to the Pyrenean mountain belt. Multiple outcrops appear in the upper reach of the valley (Ainsa sector, 50 km from headwaters) as well as in the lower reach (Albalate sector, 125 km from headwaters). Fluvial incision into bedrock was calculated using (i) differentially corrected GPS measurements of the altitude of straths and (ii) numerical dating of alluvial sediments from the lower terraces (Qt5 to Qt9) by Optically Stimulated Luminescence, previously reported by Lewis et al. (2009), and supplemented with new dates for the upper terraces (Qt1, Qt2 and Qt3) based on palaeomagnetism and supported by soil development. Considering altitude differences and the elapsed time between successive well preserved terrace couples (Qt3-Qt7, Qt7-Qt9 and Qt9-Active channel), mean bedrock incision rates ranged from 0.76 to 0.38 m ka<sup>-1</sup>, at the upper reach of the valley (Ainsa section), and from 0.61 to 0.20 m ka<sup>-1</sup>, at the lower reach (Albalate section). River incision along the valley produced vertically separated, near-parallel longitudinal terrace profiles evidencing a rapid near-uniform regional uplift as response to (i) the tectonic lithospheric thickening in NE Iberia and (ii) the erosional download rebound related to the Ebro basin exorheism. Moreover, a subtle upstream divergence of strath profiles

178  
179  
180 61 may have been a consequence of an increase in uplift rate toward the head of the  
181  
182 62 valley. Additionally, incision rates changed over time as indicate results from the lower  
183  
184 reach (Albalate section); the maximum rate was 1.48 m ka<sup>-1</sup> between Qt7 (61 ka) and  
185 63  
186 Qt8 (47 ka), and the minimum rate was 0.11 m ka<sup>-1</sup> between Qt3 (401 ka) and Qt5 (178  
187 64  
188 ka). The highest incision rates were produced after the Marine Isotope Stage 4 most  
189 65  
190 likely in response to (i) an increased snowmelt discharge during the subsequent  
191 66  
192 deglaciation related to the last maximum advance of glaciers in the southern Pyrenees,  
193 67  
194 and (ii) a limited width of the valley after Qt7 formation, resulting from the  
195 68  
196 deactivation of the westward river migration. Therefore, incision rates over the last 1  
197 69  
198 Ma in the Cinca River valley were basically controlled by near-uniform bedrock uplift,  
199 70  
200 in the context of climate variability. The results reported in this study represent  
201 71  
202 significant data on fluvial incision in NE Iberia, and provide an assessment of the  
203 72  
204 regional post-tectonic landscape evolution.  
205 73  
206  
207  
208  
209  
210

211 74 **Key words:** Fluvial incision, Staircase terraces, Uplift, Climate change, Mid- to Late  
212  
213 75 Pleistocene, Southern Pyrenees and Ebro Basin  
214  
215  
216  
217  
218  
219  
220 77  
221  
222  
223 78  
224  
225  
226  
227 79  
228  
229  
230 80  
231  
232  
233 81  
234  
235  
236

237  
238  
239 **82 1. Introduction**  
240  
241

242 83 Landscape evolution represents a morphotopographic balance resulting from  
243  
244  
245 84 interactive competition between tectonics, climate and denudation processes (e.g.,  
246  
247 85 Burbank and Anderson, 2001; Willet et al., 2006; Cloetingh and Willett, 2013). Fluvial  
248  
249 86 terraces are excellent geomorphic markers that have been used extensively to  
250  
251  
252 87 document landscape evolution (e.g., Bridgland and Westaway, 2008; Westaway et al.,  
253  
254 88 2009). Long-term geomorphic configuration of fluvial systems involves the  
255  
256 89 entrenchment of river valleys and the creation of staircase terrace sequences in  
257  
258  
259 90 response to the basic driving forces of regional climate, tectonic uplift and base level  
260  
261 91 (e.g., Bridgland, 2000; Starkel, 2003; Gibbard and Lewin, 2009; Westaway et al., 2009;  
262  
263 92 Stokes et al., 2012; Pazzaglia, 2013; Wang et al., 2015).

264  
265  
266 93 Terraces as geomorphic markers to assess fluvial incision and landscape development  
267  
268  
269 94 have been commonly used worldwide under different orogenic and post-orogenic  
270  
271 95 geodynamic contexts. At a regional scale, deciphering the nature and history of fluvial  
272  
273 96 incision in the Iberian Peninsula, which has an extensive network of terraces, has been  
274  
275  
276 97 limited and remains an unsolved challenge. Undoubtedly, the general lack of well  
277  
278 98 chronologically referenced terrace systems (Santisteban and Schulte, 2007) is  
279  
280 99 determinant. Several regional studies on river incision have been reported by Cunha et  
281  
282 100 al. (2005, 2008, 2012) and Martins et al. (2009, 2010) in the Portuguese reach of the  
283  
284 101 Tagus River, Antón et al. (2012) and Silva et al. (2013, 2016) in the Spanish reaches of  
285  
286  
287 102 the Duero and Tagus rivers, Stange et al. (2013; 2016) in the Segre River valley in the  
288  
289 103 southern Pyrenees, Soria-Jáuregui et al. (2016) in the upper sector of the Ebro River  
290  
291 104 valley, Scotti et al. (2014) and Giacheta et al. (2015) in the Iberian Ranges (NE Spain),  
292  
293  
294  
295

296  
297  
298 105 and Viveen et al. (2014) in the Miño River basin from northwest Iberian. Additionally,  
299  
300  
301 106 data on regional fluvial incision need to be integrated within the geodynamic models  
302  
303 107 explaining the Iberian topography and with the regional Pleistocene climate  
304  
305 108 reconstruction for southwestern Europe.  
306  
307

308 109 The Spanish Pyrenees and the adjacent Ebro foreland basin comprise an outstanding  
309  
310  
311 110 area to deduce post-orogenic river incision rates and landscape development from  
312  
313 111 staircase terraces and to discuss the uplift mechanisms and the climate changes  
314  
315 112 involved. In this paper we use a well characterized sequence of staircase terraces  
316  
317  
318 113 located along the Cinca River valley, one of the most important Pyrenean tributaries of  
319  
320 114 the Ebro River in northeast Iberia, to evaluate post-tectonic landscape evolution.  
321

322 115 Reported results are based in a combination of (i) reconstructed longitudinal strath  
323  
324 116 profiles starting from previously mapped terraces (Sancho, 1988), (ii) numerical ages  
325  
326 117 using optically stimulated luminescence (OSL) and supported by time-related trends in  
327  
328  
329 118 soil development (Lewis et al., 2009), and (iii) new palaeomagnetic and soil  
330  
331 119 stratigraphic data. We use our results to deduce spatial and temporal patterns in river  
332  
333 120 incision rates and to discuss the combined action of uplifting and climate change  
334  
335 121 governing the formation of staircase terrace sequences in NE Iberia.  
336  
337  
338

## 339 122 **2. Study area**

### 340 341 342 123 **2.1 The Cinca River valley**

343  
344  
345 124 The Cinca River valley straddles the south-central Pyrenees and the northern Ebro  
346  
347  
348 125 basin (NE Spain) (Figs. 1, 2A). Mean annual precipitation varies from > 2,000 mm in the  
349  
350 126 high Pyrenees to < 400 mm in the semiarid Ebro basin. The Cinca River is 170 km long;  
351  
352  
353  
354

355  
356  
357 127 it has a drainage area of 9,700 km<sup>2</sup> and a mean annual flood discharge of 79 m<sup>3</sup>/s. The  
358  
359 128 natural fluvial regime of the Cinca River is altered by the presence of two large  
360  
361  
362 129 reservoirs: the El Grado and Mediano dams (Fig. 3A).  
363  
364

365 130 The headwaters area of the Cinca River is glaciated and is located in the Pyrenean  
366  
367 131 Internal Sierras (Monte Perdido summit: 3,355 m a.s.l.). The Cinca River drains to the  
368  
369 132 south and is perpendicular to the Pyrenean belt, joining the larger and eastward-  
370  
371  
372 133 flowing Ebro River in the Ribarroja reservoir (90 m a.s.l.) in the central Ebro Basin. This  
373  
374 134 river confluence is more than 100 km up gradient from the Mediterranean Sea (Fig. 1).  
375  
376 135 The Cinca River in the upper valley (from headwaters to Ainsa; Figs. 1, 3A) is a mixed  
377  
378 136 bedrock-alluvial channel, whereas the Cinca River in the lower valley (from Basbastro  
379  
380 137 to the mouth into the Ebro River; Figs. 1, 3A) is an alluvial gravel channel. Several slight  
381  
382 138 knickpoints can be identified along the active channel profile: however, only the  
383  
384 139 knickpoint located at El Grado (External Pyrenees) is noticeable (Figs. 2B, 3A).  
385  
386  
387  
388

## 389 140 **2.2 Geologic setting**

390  
391

392 141 Geologically, the Cinca River valley is excavated in the Pyrenean belt and the adjacent  
393  
394 142 Ebro foreland basin (Fig. 2A). The Pyrenees constitutes a WNW-ESE striking, narrow  
395  
396 143 asymmetric alpine chain with a mainly southward vergence, developed from the Late  
397  
398 144 Cretaceous to the Early Miocene. This structural setting was formed in response to the  
399  
400 145 partial subduction of the Iberian lithosphere underneath Europe (e.g., Muñoz, 2002).  
401  
402 146 The southern central Pyrenees comprise part of the Axial Zone, formed by a basement  
403  
404 147 and a series of imbricated thrust sheets, involving Mesozoic to Eocene cover rocks and  
405  
406 148 affecting synorogenic Tertiary materials (e.g., Martínez-Peña and Casas-Sainz, 2003).  
407  
408  
409  
410  
411  
412  
413

414  
415  
416  
417  
418  
419  
420  
421  
422  
423  
424  
425  
426  
427  
428  
429  
430  
431  
432  
433  
434  
435  
436  
437  
438  
439  
440  
441  
442  
443  
444  
445  
446  
447  
448  
449  
450  
451  
452  
453  
454  
455  
456  
457  
458  
459  
460  
461  
462  
463  
464  
465  
466  
467  
468  
469  
470  
471  
472

149 Specifically, the Cinca River valley is located at the western border of the South  
150 Pyrenean Central Unit that is characterized by north-south oblique structures that  
control the north-south alignment of the Cinca River (Martínez-Peña et al., 1995).  
152 From a stratigraphic point of view, the Cinca River traverses the western sector of the  
153 Graus-Tremp basin (the Ainsa sub-basin) (Fig. 2B), a piggy-back basin filled with  
154 Palaeocene-Eocene deposits (Puigdefábregas and Souquet, 1986).

155 The Tertiary Ebro basin was formed during the Palaeogene as a consequence of  
flexural subsidence related to growth of the surrounding mountain chains, particularly  
156 the Pyrenees. Sedimentation into the closed basin continued under conditions of  
157 continental internal drainage during Oligocene and Miocene times (Muñoz et al., 2002;  
158 Costa et al., 2010) (Fig. 2B). This sedimentary regime persisted until the end of the late  
159 Miocene (between 12.5 and 8.5 Ma) when the internal drainage of the Ebro basin  
160 ended due to aggradation of the lacustrine system and extensional geodynamic  
161 conditions in the western Mediterranean basin (García-Castellanos et al., 2003). The  
162 Ebro basin was subsequently opened when headward erosion of coastal drainage  
163 captured the internally draining system. The Ebro sedimentary basin was then incised  
164 and previous depositional units were excavated and transported to the coastal  
165 Mediterranean.

166 Erosional activity of the drainage in the Pyrenees and the Ebro Basin persisted  
167 throughout the Quaternary. Subsequent fluvial activity developed extensive staircase  
168 terrace sequences along the Ebro drainage system (e.g., Gutiérrez and Peña, 1994;  
169 Peña, 1994). The earliest evidence of alluviation in the exoreic Ebro basin is at ca. 1.28

473  
474  
475 171 Ma in the Alcanadre River valley, a tributary of the Cinca River (Duval et al. 2015;  
476  
477  
478 172 Sancho et al., 2016).  
479  
480

### 481 173 **2.3 Approach to the Cinca River terrace sequence**

482  
483  
484 174 Two basic configurations of stream terraces, strath and fill terraces, are commonly  
485  
486 175 differentiated, based on the morphology of the erosional surface and thickness of  
487  
488  
489 176 alluvial sediments (Bull, 1991; Pazzaglia, 2013). A strath terrace is characterized by a  
490  
491 177 subhorizontal erosional surface carved into bedrock mantled with a thin mobile alluvial  
492  
493 178 cover of a bedrock channel that does not exceed the depth of scour of the stream. In  
494  
495 179 contrast, fill terraces are characterized by an irregular basal surface covered by a layer  
496  
497  
498 180 of thick alluvium that accumulates when the channel vertically exceeds the depth of  
499  
500 181 scour, during periods of valley aggradation (Wegmann and Pazzaglia, 2009; Pazzaglia,  
501  
502 182 2013). The thickness of the alluvial cover is a long-discussed criterion to distinguish  
503  
504 183 between both types of terrace (Pazzaglia, 2013). Mobile alluvial cover associated with  
505  
506  
507 184 strath terraces rarely exceeds 5 m in thickness even for large watersheds, while  
508  
509 185 greater alluvial thickness is usually related to fill terraces (Pazzaglia, 2013).  
510  
511

512 186 The studied terrace sequence in the Cinca River valley consists of 10 extensive paired  
513  
514 187 cyclic stream terraces (Sancho, 1988; Lewis et al., 2009). The mean thickness of the  
515  
516  
517 188 alluvial mantle covering the straths is around 5 m, ranging from 8 m for the oldest  
518  
519 189 terraces to 3 m for the youngest terraces. The general morphology of strath surfaces is  
520  
521 190 broadly subhorizontal. Given this description, the Cinca River terrace sequence is  
522  
523  
524 191 closer to a strath relative to a fill terrace and displays a strath-like terrace. We  
525  
526  
527  
528  
529  
530  
531

532  
533  
534 192 recognize that in places, a near-fill terrace configuration related to slight valley  
535  
536  
537 193 aggradations could be considered.  
538  
539

### 540 194 **3. Methods: using terrace straths to measure river incision**

541  
542  
543 195 Determination of the river incision rate (e.g., Burbank and Anderson, 2001) for a point  
544  
545 196 along a river valley is given by the ratio between the height (m) of the terrace strath  
546  
547 above the active channel and the timing (ka) of terrace formation. We expanded this  
548 197 approach to calculate the river incision rate between a given pair of terraces; the  
549  
550 198 fluvial incision rate ( $I_{Q_{ti}-Q_{tj}}$ ) (m/ka) between any two terraces  $Q_{ti}$  and  $Q_{tj}$ , is given by the  
551  
552 199 relation:  
553  
554 200  
555  
556

$$558 \quad 201 \quad I_{Q_{ti}-Q_{tj}} = H_{Q_{ti}-Q_{tj}} / T_{Q_{ti}-Q_{tj}}$$

559  
560  
561 202 where  $H_{Q_{ti}-Q_{tj}}$  is the difference of altitude (m) of the terrace straths  $Q_{ti}$  and  $Q_{tj}$ , and  
562  
563 203  $T_{Q_{ti}-Q_{tj}}$  is the elapsed time (ka) between them.  
564  
565  
566

567 204 We use the terrace straths rather than the terrace treads to measure river incision  
568  
569 205 rates (Wegmann and Pazzaglia, 2009) because tread surfaces can be subsequently  
570  
571 206 modified through both aggradation or degradation. Observations of terrace  
572  
573 207 stratigraphy indicate that in places the terrace surface has been aggraded through  
574  
575 deposition of lateral alluvial and aeolian sediments or degraded through erosion  
576 208  
577 removal and lowering of the original terrace surface as indicated by severely truncated  
578 209  
579 or missing soil profiles.  
580 210  
581  
582

#### 583 211 **3.1 Height of terrace straths and the active channel**

584  
585  
586  
587  
588  
589  
590

591  
592  
593  
594  
595  
596  
597  
598  
599  
600  
601  
602  
603  
604  
605  
606  
607  
608  
609  
610  
611  
612  
613  
614  
615  
616  
617  
618  
619  
620  
621  
622  
623  
624  
625  
626  
627  
628  
629  
630  
631  
632  
633  
634  
635  
636  
637  
638  
639  
640  
641  
642  
643  
644  
645  
646  
647  
648  
649

212 Collecting and assessing height measurements of bedrock strath surfaces requires  
213 compiling a detailed regional geomorphological framework. Geomorphic mapping was  
214 undertaken on an aerial photographic base (1:18,000 in scale) and was extensively  
215 field checked along the Cinca River valley. Ten terraces were firstly identified (Qt1 to  
216 Qt10, from higher to lower) from their altitudinal position (Sancho, 1988; Lewis et al.,  
217 2009). Correlation of terraces was primarily based on geomorphologic and  
218 stratigraphic relationships between terraces and was reinforced with soil development  
219 and numerical dating. Elevations of the differentiated strath terrace surfaces and the  
220 Cinca active channel were measured to sub-meter accuracy using a global positioning  
221 system (GPS) differentially corrected to a permanent base station. Measurements  
222 were occasionally supplemented by data from 1:25,000-scale topographic maps.  
223 Height measurements allowed reconstruction of accurate profiles of strath terraces  
224 and the active channel.

### 3.2 Chronology of terraces

226 Timing of strath preservation is broadly based on the basal age of overlying fluvial  
227 deposits. We used numerical dates previously provided by Lewis et al. (2009), based on  
228 OSL of quartz grains dating and supported by soil stratigraphy. These data are available  
229 only for the lower terraces (from Qt5 to Qt9) corresponding to both the Penultimate  
230 and the Last Glacial cycles. In this study we provide new chronological evidence for the  
231 older terraces using paleomagnetic analysis and time-related trends in soil  
232 development.

#### 3.2.1 Paleomagnetic sampling and laboratory procedures

650  
651  
652 234 Characterization of the paleomagnetic polarity has been a powerful tool for unravelling  
653  
654 235 terrace ages since the pioneering work of Pevzner (1970). Subsequent applications  
655  
656  
657 236 have focused on locating the Brunhes/Matuyama (B/M) boundary (Dubar and Semah,  
658  
659 237 1986; Jacobson et al., 1988) or even shorter polarity events within the Brunhes and  
660  
661 238 Matuyama periods (Li et al., 1997). Paleomagnetic analysis was conducted on the Cinca  
662  
663 239 River alluvium overlying the strath terraces to identify the location of the B/M  
664  
665 240 boundary. Previous results in the Central Ebro Basin (Gil et al., 2013) and in the  
666  
667 Alcanadre River (tributary of the Cinca River; Calle et al., 2015; Sancho et al., 2016)  
668 241  
669 allowed us to be confident of the suitability of the method provided that an adequate  
670 242  
671 sampling was guaranteed (Gil Garbi, 2017).  
672 243  
673  
674  
675 244 Sampling for paleomagnetic analysis was performed in 13 pits excavated in the upper  
676  
677 terraces along the valley (from Qt1 to Qt7). Siltstone layers within alluvial sequences  
678 245  
679 were the main targets to ensure a stable paleomagnetic signal. Sampling tools  
680 246  
681 designed for unconsolidated sediments were used instead standard drilling machines.  
682 247  
683 Subsequent consolidating techniques using non-magnetic chemical compounds  
684 248  
685 (sodium silicate and alumina cement) were used to obtain standard and stable  
686 249  
687 paleomagnetic specimens (Pueyo et al., 2006). Oriented blocks were occasionally  
688 250  
689 sampled.  
690 251  
691  
692  
693  
694 252 Present-day declination ( ~ 1° 30'W) during the sampling was corrected in the core  
695  
696 orientations (NOAA's National Geophysical Data Center, <https://www.ngdc.noaa.gov/>).  
697 253  
698 Stepwise and detailed demagnetisation (both thermal [TH] and alternating field [AF])  
699 254  
700 was conducted in the paleomagnetic laboratory at the University of New Mexico  
701 255  
702 (UNM) (Albuquerque) and at the Institute of Earth Sciences "Jaume Almera" (Consejo  
703 256  
704  
705  
706  
707  
708

709  
710  
711 Superior de Investigaciones Científicas-Universitat de Barcelona). TH demagnetisation  
712 257  
713 was run with a TSD-1 furnace (Shonsted Ltd.), and remanent magnetization was  
714 258  
715 measured with a 2G three-axis SQUID magnetometer in both laboratories. The 2G-AF  
716 259  
717 demagnetizer was only used in the UNM laboratory.  
718 260  
719

720  
721 Thermal stepwise demagnetisation used intervals of 50°C between room temperature  
722 261  
723 and 550-600°C and AF increments between 3 and 10 mT up to 100mT (following an  
724 262  
725 exponential trend) were run to characterize all paleomagnetic components of the  
726 263  
727 NRM. Paleomagnetic directions were fitted by principal components analysis (PCA;  
728 264  
729 Kirschvink, 1980) using the Paldir software by Utrecht Universiteit. In some cases,  
730 265  
731 demagnetization circles (Bailey and Halls, 1978), the stacking routine (Scheepers and  
732 266  
733 Zijdeveld, 1992) and the virtual directions method (Ramón and Pueyo, 2017) were  
734  
735 267  
736 used to double-check the PCA results. Site means and terrace means were fitted by  
737 268  
738 Fisher (1953) statistics. It is a probability distribution for multivariate directional data  
739 269  
740 (vectors or simple lines in the 3D space).  
741  
742 270  
743  
744

745 271 *3.2.3 Soil development*  
746  
747

748 272 Soil development indices were used locally and regionally to correlate principal terrace  
749  
750 levels (Lewis et al., 2009) and to estimate the age of the Qt3 terrace. Soils were  
751 273  
752 described according to standard methods and nomenclature of the U.S. Soil Survey  
753 274  
754 Staff (1993). Carbonate stage morphology follows nomenclature of Gile et al. (1981)  
755 275  
756 and Birkeland (1999). Time-related changes in soil morphology were analyzed using a  
757 276  
758 well-tested soil development index (SDI) (Harden, 1982; Harden and Taylor, 1983;  
759  
760 277  
761 McDonald et al., 1996) based on a soil chronofunction presented in Lewis et al. (2009).  
762 278  
763  
764  
765  
766  
767

768  
769  
770 279 SDI values were calculated using a conversion of soil morphologic properties  
771  
772 280 (rubification, texture, structure, dry consistence, moist consistence, secondary  
773  
774 carbonates, lightening, and argillans) into numerical data to enable a quantitative  
775 281 comparison of the degree of soil development. Horizon Development Index (HDI)  
776  
777 282 values are obtained by normalizing each set of properties and a Profile Development  
778  
779 283 Index (PDI) is calculated from HDI values and horizon thickness. The PDI values reflect  
780  
781 284 the overall degree of soil development and provide a means of comparison among  
782  
783 285 soils within a given sequence or area. The PDI has proven useful for providing  
784  
785 286 correlations and calibrated age estimates for the sequence of strath terraces from the  
786  
787 287 Cinca River valley (Lewis et al., 2009).  
788  
789  
790  
791 288

## 792 793 794 289 **4. Results**

### 795 796 797 290 ***4.1 Morphopedosedimentary characteristics of the staircase terrace sequence***

798  
799 291 The marked vertical separation between adjacent terraces, reinforced with extensive  
800  
801 292 outcrops and their longitudinal continuity, facilitated mapping, regional correlation of  
802  
803 293 terrace remnants, and descriptions of the fluvial terrace deposits along 170 km in the  
804  
805 294 Cinca River valley (Figs. 3, 4). Ten paired staircase terraces (numbered Qt1, Qt2, Qt3,  
806  
807 295 Qt4, Qt5, Qt6, Qt7, Qt8, Qt9, and Qt10, from oldest to youngest) have been preserved  
808  
809 296 (Appendix 1). The terrace development and preservation are prominently displayed in  
810  
811 297 the upper reach of the valley (near Ainsa, 50 km from the headwaters) and  
812  
813 298 immediately downstream of the confluence with the Ara River (Figs. 3B, 4A, D). Mean  
814  
815 299 height of the terrace straths above the active channel of the Cinca River in this sector  
816  
817 300 are 172.5 m (Qt3), 44.2 m (Qt7) and 6.0 m (Qt9) (Table 1). The corresponding vertical  
818  
819  
820  
821  
822  
823  
824  
825  
826

827  
828  
829  
830  
831  
832  
833  
834  
835  
836  
837  
838  
839  
840  
841  
842  
843  
844  
845  
846  
847  
848  
849  
850  
851  
852  
853  
854  
855  
856  
857  
858  
859  
860  
861  
862  
863  
864  
865  
866  
867  
868  
869  
870  
871  
872  
873  
874  
875  
876  
877  
878  
879  
880  
881  
882  
883  
884  
885

301 separations between adjacent preserved strath terraces are 128.3 m (Qt3-Qt7) and  
302 38.2 m (Qt7-Qt9) respectively.

303 The lower reach of the valley goes from the External Pyrenees, where the Cinca River  
304 enters into the Ebro Basin, to the confluence with the Ebro River, including several  
305 important tributary junctions (the Esera, Vero and Alcanadre rivers). The lower reach  
306 shows the widest and best preserved terraces (Fig. 4B, E, F), particularly in the  
307 Albalate-Belver sector (125 km from the headwaters; Fig. 3C). Mean height of the  
308 terrace straths above the active channel of the Cinca River in this sector are 182.1 m  
309 (Qt1), 132.5 m (Qt2), 103.5 m (Qt3), 91.3 m (Qt4), 79.9 m (Qt5), 60.4 m (Qt6), 33.9 m  
310 (Qt7), 13.1 m (Qt8) and 3.6 m (Qt9) (Table 1). The corresponding vertical separations  
311 between adjacent strath terraces are 49.6 m (Qt1-Qt2), 29.0 m (Qt2-Qt3), 12.2 m (Qt3-  
312 Qt4), 11.4 m (Qt4-Qt5), 19.5 m (Qt5-Qt6), 26.5 m (Qt6-Qt7), 20.8 m (Qt7-Qt8) and 9.5  
313 m (Qt8-Qt9).

314 Terraces Qt3, Qt7 and Qt9 are broadly preserved along the Cinca River valley  
315 (Appendix 1). Terraces older than Qt7 are preserved only on the river's east bank,  
316 indicating the westward migration of the Cinca River. This migration is well noted in  
317 the Albalate-Belver sector and reaches a lateral westward displacement of 8 km  
318 between Qt1 at Monte Julia and Qt7 at Albalate (Fig. 3C). Qt7 and subsequent Qt8 and  
319 Qt9 terraces outcrop in both sides of the valley. This implies a significant change in the  
320 width of the valley. In fact, Qt7 is approximately 5 km wide in the Albalate-Alcolea  
321 section, whereas the current valley bottom (active channel and floodplain) reaches a  
322 maximum width of 2 km (Fig. 3C).

886  
887  
888  
889  
890  
891  
892  
893  
894  
895  
896  
897  
898  
899  
900  
901  
902  
903  
904  
905  
906  
907  
908  
909  
910  
911  
912  
913  
914  
915  
916  
917  
918  
919  
920  
921  
922  
923  
924  
925  
926  
927  
928  
929  
930  
931  
932  
933  
934  
935  
936  
937  
938  
939  
940  
941  
942  
943  
944

323 Terrace treads are typically broad (2-4 km width) and commonly underlain by 2.8-7.7  
324 m (Fig. 4C) of largely cobble-rich gravel with a sand-rich matrix, large (20-100 cm  
325 diameter) sub-rounded boulders, sparsely populated with sand lenses, and capped by  
326 either gravelly sand-rich alluvium or finer-textured overbank deposits. Fluvial deposits  
327 occur in fining-upwards sequences. According to lithofacies of Miall (1978), gravels are  
328 generally massive but locally imbricated (Gm) and cross-stratified (Gt, Gp), are well-  
329 sorted and sub-rounded and consist of limestone, sandstone, granite, quartzite, and  
330 schist (in order of decreasing abundance) of Pyrenean and, locally, Ebro basin  
331 provenances. Interbedded sand lenses can be cross-stratified (St, Sp) or horizontally  
332 laminated (Sh). Gravels can be capped by overbank silts (Fm).

333 Strath surfaces are carved into Cretaceous to Eocene marine carbonates and marls  
334 (Fig. 4A) along the river's Pyrenean reach and Eocene-Miocene continental deposits  
335 (Fig. 4B) along the Ebro Basin reach (Fig. 2B; Appendices 1 and 2). Localized  
336 deformation of the strath surface and associated gravels (e.g., tilting and faulting)  
337 occurs in places and is related to salt diapirism and gypsum dissolution confined to the  
338 Barbastro anticline and the Estada-Estadilla diapir (Sancho, 1988, 1989; Lucha et al.,  
339 2008) (Appendix 1). Local deformation related to small vertical faults was also  
340 observed near El Grado and El Pueyo de Araguás.

341 The Qt1 terrace is poorly preserved and only occurs between Albalate and Binaced  
342 (Figs. 3C, 4F; Appendix 1), where remnants occur as isolated hills (San Salvador and Las  
343 Brujas sites). The Qt1 remnants constitute the highest preserved remnants of the Cinca  
344 River terrace sequence. Mean thickness of alluvial cover is around 7.7 m and maximum  
345 grain size (Dmax) ranges from 30-48 cm (mean value  $42\pm 9$  cm) (Appendix 2). An

945  
946  
947  
948 346 eroded petrocalcic soil horizon ( ~1 m thick) formed in fine-grained sediments is  
949  
950 347 preserved in places.

951  
952  
953 348 The Qt2 strath terrace is more or less continuously preserved between Albalate and  
954  
955 Belver and is in the vicinity of the Qt1 remnants (Figs. 3C; Appendix 1). Mean thickness  
956 349 of alluvial cover preserved is around 5.6 m and maximum grain size (Dmax) ranges  
957  
958 350 from 36-48 cm (mean value  $41\pm 4$  cm) (Appendix 2). The soils found on the Qt2 are only  
959  
960 351 weakly to moderately developed and are considerably less developed than the soils on  
961  
962 352 the younger Qt3 terrace. This indicates that the original terrace surface has been  
963  
964 353 severely eroded.

965  
966  
967 354  
968  
969  
970 355 The Qt3 terrace is one of the two most important geomorphic features along the Cinca  
971  
972 356 River valley. It is preserved continuously in the lower reach of the valley between  
973  
974 Monzón and Fraga (Figs. 3C, 4F; Appendix 1); other relevant outcrops have been  
975 357 identified at Barbastro, El Grado and Ainsa (Figs. 3B, 4D; Appendix 1). Mean thickness  
976  
977 358 of alluvial cover is around 5.8 m and maximum grain size (Dmax) ranges from 26-50 cm  
978  
979 359 (mean value  $34\pm 6$  cm) (Fig. 5; Appendix 2). Locally the Qt3 deposit near El Grado is  
980  
981 360 faulted. Soil characteristics on this terrace are described below.

982  
983 361  
984  
985  
986  
987 362 The Qt4 terrace is preserved only between Barbastro and Fraga (Figs. 3C, 4E; Appendix  
988  
989 363 1). Mean thickness of alluvial cover is around 5.2 m and maximum grain size (Dmax)  
990  
991 364 ranges from 26-43 cm (mean value  $35\pm 8$  cm) (Appendix 2). Near Belver, the terrace  
992  
993 deposits include a 90 cm-thick aeolian cap that overlies 90 cm of overbank fines. An  
994 365 OSL date on the loess cap constrains its age to be  $20\pm 3$  ka (Lewis et al., 2009), likely  
995  
996 366 deposited during the MIS2 glaciation. No soils were described on the Qt4 terrace due  
997  
998 367

1004  
1005  
1006  
1007 368 to surface erosion. In some localities, reworking of the Qt4 surface is evidenced by a  
1008  
1009 369 cap of colluvium incorporating pieces of underlying petrocalcic horizons.  
1010  
1011

1012 370 The Qt5 terrace is also preserved only between Monzón and Fraga Fraga (Fig. 3C;  
1013  
1014 371 Appendix 1). Stratigraphic relations between the Qt4 and Qt5 terraces indicate that  
1015  
1016 372 formation of the Qt5 terrace cannibalized much of the older Qt4 terrace. Mean  
1017  
1018  
1019 373 thickness of alluvial cover is around 4.5 m and maximum grain size (Dmax) ranges from  
1020  
1021 374 28-51 cm (mean value  $38\pm 7$  cm) (Appendix 2). North of Castejón del Puente, the Qt5  
1022  
1023 375 terrace was deformed by the diapiric activity of the Barbastro salt anticline (Sancho,  
1024  
1025  
1026 376 1989). The Qt5 soils in the Albalate sector have well developed Bk and Bkm horizons  
1027  
1028 377 with stage III+ to IV+ carbonate morphology (Table 2) (Lewis et al., 2009).  
1029  
1030

1031 378 The Qt6 terrace is also preserved only between Monzón and Fraga Fraga (Figs. 3C;  
1032  
1033 379 Appendix 1) and exposures of the deposits are very limited because the degradation of  
1034  
1035  
1036 380 the scarps. Mean thickness of alluvial cover is around 5.1 m and maximum grain size  
1037  
1038 381 (Dmax) ranges from 24-80 cm (mean value  $39\pm 19$  cm) (Appendix 2). Soils have a well-  
1039  
1040 382 developed Btk horizon and stage III+ carbonate morphology (Table 2) (Lewis et al.,  
1041  
1042 383 2009).  
1043  
1044

1045  
1046 384 Remnants of the Qt7 terrace occur continuously along approximately 120 km of the  
1047  
1048 385 Cinca valley (Figs. 3B, C, 4; Appendix 1). This is the best-preserved terrace on the Cinca  
1049  
1050 386 and the most relevant terrace marker in the landscape. Terrace remnants are broad  
1051  
1052 387 and up to 4 km in width along the lower reach. Mean thickness of alluvial cover is  
1053  
1054  
1055 388 around 5 m. Maximum grain size (Dmax) ranges from 20-68 cm (mean value  $34\pm 9$  cm)  
1056  
1057 389 (Fig. 5; Appendix 2). Local distribution of terraces in the Albalate area suggests that  
1058  
1059  
1060  
1061  
1062

1063  
1064  
1065  
1066 390  
1067  
1068 391  
1069  
1070 392  
1071  
1072 393  
1073  
1074 394  
1075  
1076  
1077 395  
1078  
1079 396  
1080  
1081 397  
1082  
1083  
1084  
1085 398  
1086  
1087 399  
1088  
1089 400  
1090  
1091 401  
1092  
1093  
1094 402  
1095  
1096 403  
1097  
1098  
1099 404  
1100  
1101 405  
1102  
1103  
1104 406  
1105  
1106 407  
1107  
1108 408  
1109  
1110 409  
1111  
1112  
1113 410  
1114  
1115 411  
1116  
1117  
1118  
1119  
1120  
1121

Qt7 terrace formation cannibalized much of older Qt6 and Qt5 terraces. In some locations, there is 3-4 m of colluvium on top of the Qt7 fluvial deposits. The Qt7 strath surface and overlying deposits are deformed when the underlying bedrock is composed of Upper Triassic evaporites and clays (Estada-Estadilla diapir) and Eocene evaporites (Barbastro salt anticline) (Sancho, 1989; Lucha et al., 2008). Local small faults deform the Qt7 deposits at El Pueyo de Araguás. The Qt7 soils in the Albalate sector have moderately to well-developed Btk horizons and stage II to weak stage III carbonate morphology (Table 2) (Lewis et al., 2009).

The Qt8 terrace is not as extensively preserved as Qt7; it crops out only along the lower 35 km of the valley (Fig. 3C; Appendix 1), where it is 2-3 km wide. Mean thickness of alluvial cover is around 2.7 m and maximum grain size ( $D_{max}$ ) ranges from 22-42 cm (mean value  $29 \pm 6$  cm) (Appendix 2). Soils in the Albalate sector have moderately developed Btk horizons with stage II carbonate morphology (Table 2) (Lewis et al., 2009).

The Qt9 terrace is generally co-extensive with the Qt7 terrace and traceable along 140 km of the total length of the river valley (Figs. 3B, C, 4D, E, F; Appendix 1). The Qt9 terrace is also largely co-extensive with Qt8, where the latter is preserved, and is approximately 2 km wide. Maximum grain size ( $D_{max}$ ) ranges from 12-60 cm (mean value  $29 \pm 12$  cm) (Fig. 5; Appendix 2) and mean thickness of alluvial cover is around 3.3 m. Locally this terrace is considerably thicker (e.g., 10 m at Castejón del Puente) because of deposition across the synsedimentary karstic subsidence on the south flank of the Barbastro salt anticline. The Qt9 soils in the Albalate sector have moderately

1122  
1123  
1124  
1125<sup>412</sup> developed Bw and Bk horizons with stage I+ carbonate morphology (Table 2) (Lewis et  
1126  
1127<sup>413</sup> al., 2009).

1128  
1129  
1130<sup>414</sup> The Qt10 terrace (Figs. 3B, C, 4E, F), which is in an extensive active floodplain, has  
1131  
1132<sup>415</sup> Roman bridge abutments preserved on its top near Castejón del Puente,  
1133  
1134  
1135<sup>416</sup> demonstrating that this has been the active surface since at least Roman times in the  
1136  
1137<sup>417</sup> region (from ca. 140 BC until ca. 400 AD, approximately about 2,000 years ago)  
1138  
1139<sup>418</sup> (Beltrán, 1985).

#### 1140 1141 1142<sup>419</sup> **4.2 Terrace profiles** 1143

1144  
1145  
1146<sup>420</sup> The longitudinal profiles of the terrace straths and the active channel of the Cinca  
1147  
1148<sup>421</sup> River were reconstructed (Fig. 6) from 300 GPS measurements (Appendices 1 and 2)  
1149  
1150<sup>422</sup> and a few elevations derived from topographic maps. Strath heights (projected to a  
1151  
1152<sup>423</sup> common vertical plane down the center of the modern stream valley) reveal several  
1153  
1154  
1155<sup>424</sup> consistent patterns along the length of the Cinca River from headwaters to its  
1156  
1157<sup>425</sup> confluence with the Ebro River. Several key features of the terrace profiles are  
1158  
1159<sup>426</sup> significant.

1160  
1161  
1162  
1163<sup>427</sup> First, the Cinca River has experienced progressive fluvial incision subsequent to  
1164  
1165<sup>428</sup> formation of the Qt1 terrace, producing a marked vertical separation among terraces  
1166  
1167<sup>429</sup> (Fig. 6; Table 1). As a consequence, a noticeable and well expressed staircase pattern  
1168  
1169<sup>430</sup> has developed along the valley.

1170  
1171  
1172  
1173<sup>431</sup> Second, overall longitudinal profiles are semi-parallel with a slight, but clear, upstream  
1174  
1175<sup>432</sup> divergence (Fig. 6). The greatest expression of divergence is recorded by the Qt3  
1176  
1177<sup>433</sup> terrace with vertical separation between the active channel and strath surface ranging  
1178  
1179  
1180

1181  
1182  
1183  
1184<sup>434</sup> from 165-175 m near Ainsa (km 50), 130-135 m at Barbastro (km 100) and 95-105 m at  
1185  
1186<sup>435</sup> Zaidín (km 155). Locally variable effects in divergence are observed along the profile  
1187  
1188<sup>436</sup> due to rock resistance, active faulting, and gypsum diapirism and dissolution; however,  
1189  
1190<sup>437</sup> these effects cannot explain the first-order longitudinal trends. The Qt7 profile also  
1191  
1192<sup>438</sup> diverges upstream with respect to the active channel, although not as markedly. For  
1193  
1194  
1195<sup>439</sup> example, the Qt7 is 45-50 m above the active channel near Ainsa, 40 m at Barbastro  
1196  
1197<sup>440</sup> and 30-35 m near Zaidín.

1198  
1199  
1200<sup>441</sup> The log plot of longitudinal profiles also shows changes in gradient at the Pyrenean  
1201  
1202  
1203<sup>442</sup> mountain front. A prominent knickpoint occurs in the active channel at 90 km from the  
1204  
1205<sup>443</sup> headwaters near El Grado (Fig. 6). This knickpoint is related to the higher erosional  
1206  
1207<sup>444</sup> resistance of the folded rocks (Cretaceous and Eocene limestones) of the External  
1208  
1209<sup>445</sup> Pyrenees (Fig. 2B; Appendix 1), as opposed to less resistant clastic sedimentary rocks  
1210  
1211  
1212<sup>446</sup> at the margin of the Ebro basin. The knickpoint appears to be spatially fixed because its  
1213  
1214<sup>447</sup> location has persisted through time for straths associated with Qt3, Qt7, Qt9 terraces  
1215  
1216<sup>448</sup> and the active channel.

### 1217 1218 1219<sup>449</sup> **4.3 Terrace chronology**

#### 1220 1221 1222 1223<sup>450</sup> **4.3.1 Geochronology for terraces Qt5 to Qt9**

1224  
1225  
1226<sup>451</sup> Numerical ages of the five youngest terraces (Qt5, Qt6, Qt7, Qt8, and Qt9) (Table 3) of  
1227  
1228<sup>452</sup> the Cinca River sequence have been previously reported by Lewis et al. (2009), from  
1229  
1230  
1231<sup>453</sup> multiple OSL dates and reinforced using regional soil stratigraphy. To summarize, Lewis  
1232  
1233<sup>454</sup> et al. (2009) obtained two dates for Qt5 terrace ( $171 \pm 22$  ka and  $180 \pm 12$  ka), giving a  
1234  
1235<sup>455</sup> weighted mean age of  $178 \pm 21$  ka, and one date for Qt6 ( $97 \pm 16$  ka). Six samples from  
1236  
1237  
1238  
1239

1240  
1241  
1242  
1243<sup>456</sup> Qt7 terrace constitute a tightly grouped set of dates ( $63 \pm 12$ ,  $59 \pm 13$ ,  $64 \pm 13$ ,  $61 \pm 3$ ,  
1244  
1245<sup>457</sup>  $56 \pm 4$  and  $65 \pm 5$ ) with a weighted mean age of  $61 \pm 4$  ka. Five dates on Qt8 terrace ( $39$   
1246  
1247<sup>458</sup>  $\pm 5$ ,  $42 \pm 6$ ,  $47 \pm 4$ ,  $50 \pm 4$  and  $50 \pm 3$ ) gave a weighted mean age of  $47 \pm 4$  ka. Finally,  
1248  
1249<sup>459</sup> eight well grouped OSL dates for Qt9 terrace gave a weighted mean age of  $11 \pm 1$  ka.  
1250  
1251<sup>460</sup> The Qt7 terrace is correlated with glacial and fluvioglacial deposits in the Cinca  
1252  
1253  
1254<sup>461</sup> headwaters (confluence of the Cinca and Cinqueta rivers at Mesón de Salinas) (Fig. 3A)  
1255  
1256<sup>462</sup> that have a mean age of  $64 \pm 11$  ka, corresponding to the last maximum glacier  
1257  
1258<sup>463</sup> extension in the south-central Pyrenees (Sancho et al., 2003). More detailed  
1259  
1260<sup>464</sup> information from OSL measurements and derivation of mean terrace deposit dates is  
1261  
1262  
1263<sup>465</sup> presented in Lewis et al. (2009).

#### 1264 1265 1266<sup>466</sup> 4.3.2 Paleomagnetic data

1267  
1268  
1269<sup>467</sup> The intensity of the NRM from terrace deposits of the Cinca River ranged in intensity  
1270  
1271  
1272<sup>468</sup> from 0.132 to 317 mA/m with an average of 39.98 mA/m ( $\pm 3.8$  mA/m), although 90%  
1273  
1274<sup>469</sup> of the data were between 0.4 and 200 mA/m (Fig. 7A). After spurious components at  
1275  
1276<sup>470</sup> very low temperatures (below 200°C), with occasional large intensities, stable  
1277  
1278<sup>471</sup> paleomagnetic directions were observed between 250 °C and 560-600 °C in the  
1279  
1280  
1281<sup>472</sup> thermal treatment (Fig. 7B). Alternating field treatment was not as successful in  
1282  
1283<sup>473</sup> isolating stable directions, although some reliable directions (comparable to TH sister  
1284  
1285<sup>474</sup> samples) were identified from 8-10 mT up to 40 mT (and even 80 mT; see for example  
1286  
1287<sup>475</sup> samples 77a and 77b) (Fig. 7B). The primary and stable component of the magnetic  
1288  
1289  
1290<sup>476</sup> field is characterized by low-coercivity and medium-temperature minerals pointing to  
1291  
1292<sup>477</sup> magnetite as the main carrier of the magnetization.  
1293  
1294  
1295  
1296  
1297  
1298

1299  
1300  
1301 478 Lower and intermediate terraces (from Qt9 to Qt3) unambiguously registered normal  
1302 polarity of the primary paleomagnetic field (Fig. 7C). On the other hand, the high level  
1303  
1304 479 Qt2 terrace unequivocally recorded a reversed polarity. This crucial observation is well  
1305 supported by the consistent directions obtained in three different pits (T9-1, T9-2 and  
1306 480 T9-3) in the Mombrún area (near Albalate) (Table 4). The oldest terrace (Qt1) recorded  
1307 an intermediate pattern, displaying both polarities and scattered directions, although  
1308 481  
1309  
1310 482  
1311  
1312  
1313 483  
1314 only one pit was sampled in this terrace. Paleomagnetic directions found in the Cinca  
1315 484  
1316 terrace sequence, therefore, are consistent (equal demagnetization intervals and  
1317 485  
1318 carriers), display pseudo-antipodal polarities (N: 355, 58 [ $\alpha_{95}$ : 10.6° and k: 5.7]; R:  
1319 486  
1320 220, -48 [ $\alpha_{95}$ : 20.6° and k: 5.74]) and seem to be a reliable record of the primary  
1321 487  
1322  
1323 paleomagnetic field (Fig. 7C).

1324 488  
1325  
1326  
1327 489 Despite individual paleomagnetic means that were weakly defined partially due to the  
1328 small number of demagnetized samples (Table 4), the mean directions and polarities  
1329 490  
1330 were consistent among the different samples sites across the same terrace. Besides,  
1331  
1332 491  
1333 the stereographic projection merging all data together gives robust and pseudo-  
1334 492  
1335 antipodal means that allow us to be confident about the primary character of the  
1336 493  
1337 magnetic record.  
1338 494  
1339  
1340  
1341

1342 495 In view of these results, a relative chronology can be established (Table 1). All studied  
1343 terraces younger than Qt3 display a normal polarity and belong to the Brunhes period  
1344 496  
1345 in agreement with the available OSL dates for Qt5 to Qt9. The Qt2 terrace must belong  
1346 497  
1347 to the Matuyama reverse period, likely close to the Brunhes/Matuyama reversal, and  
1348  
1349 498  
1350 its boundary (C1r/C1n: 0.773 Ma) (Singer, 2014) must be located between the Qt3 and  
1351 499  
1352 Qt2 terraces. The poor results found in the Qt1 terrace prevent the proposal of any  
1353 500  
1354  
1355  
1356  
1357

1358  
1359  
1360 501 reliable interpretation, although they point to the occurrence of another zone with  
1361  
1362 normal polarity. Future chronologic studies may shed light on interpretation and  
1363 502  
1364 distinguish between Jaramillo and Cobb Mt. normal events. These two hypotheses  
1365 503  
1366 have been recently proposed in other locations in the Ebro Basin (Sancho et al. 2016;  
1367 504  
1368 Gil et al., in review).  
1369 505  
1370  
1371

#### 1372 1373 506 *4.3.4 Qt3 soil characteristics and estimated soil age*

1374  
1375  
1376 507 Soils formed on the Qt3 surfaces along the upper (Ainsa) and lower (Albalate) reaches  
1377  
1378 508 of the Cinca River valley have the strongest degree of development relative to soils  
1379  
1380 formed on the younger terraces (Table 2). Soils on the Qt3 terrace near Albalate vary  
1381 509  
1382 in development, reflecting soils that have formed in either the original cobble-gravel  
1383 510  
1384 bar deposits or in the original channel settings where the soil parent material consist of  
1385 511  
1386 fine-textured overbank (with possible aeolian contributions) that overlies gravel-rich  
1387 512  
1388 alluvium. Soils formed in depositional bars have weakly developed Btk horizons that  
1389 513  
1390 overlie well-developed Bkm horizons with Stage IV to V carbonate morphology. Soils  
1391  
1392 514  
1393 formed in channel settings have weak- to moderately-developed Btk horizons with  
1394 515  
1395 stage IV carbonate morphology. Soil depth to the Bkm horizons ranges from 35 to 88  
1396 516  
1397 cm and occurs at a shallower depth for soils formed in bar deposits. Soil PDI (profile  
1398 517  
1399 development index) values range from 61.4 to 80.8 for the Qt3 soils (Table 2).  
1400  
1401 518  
1402  
1403

1404 519 By comparison, soils formed on the Qt3 terrace surface near Ainsa reflect soil  
1405  
1406 formation under a much wetter subhumid climate. Soil development primarily consists  
1407 520  
1408 of very thick soil Bt horizons with patchy to nearly continuous coatings of clay along  
1409 521  
1410 pores, ped faces and gravels. B horizon thickness on the Qt3 surface exceeds 300 cm.  
1411 522  
1412  
1413  
1414  
1415  
1416

1417  
1418  
1419  
1420<sup>523</sup> There is no carbonate accumulation in Qt3 terrace soils along the upper reach of the  
1421  
1422<sup>524</sup> Rio Cinca valley due to the high effective soil moisture. The only soil described on the  
1423  
1424<sup>525</sup> Qt3 surface near Ainsa has a PDI value of 105.1 (Table 2). The higher value reflects the  
1425  
1426<sup>526</sup> greater degree of soil development that has occurred under the more humid climate at  
1427  
1428  
1429<sup>527</sup> Ainsa sector relative to soils forming near the Albalate sector.

1430  
1431  
1432<sup>528</sup> Soil age estimates for the Qt3 were based on the soil chronofunction developed by  
1433  
1434<sup>529</sup> Lewis et al. (2009) and the PDI values calculated for the five soils described near  
1435  
1436<sup>530</sup> Albalate. We did not include the Ainsa Qt3 soil because its more humid soil  
1437  
1438  
1439<sup>531</sup> environment is not compatible with the soil chronofunction developed for soils in  
1440  
1441<sup>532</sup> more arid settings. Soil age estimates (based on each PDI value; Table 2) ranged from  
1442  
1443<sup>533</sup> 291 to 565 ka; mean age was 401±117 ka (Table 1). The Qt3 soils were better  
1444  
1445<sup>534</sup> developed than soils formed on the Qt5 surface, which is approximately 178 ka (Table  
1446  
1447  
1448<sup>535</sup> 2).

#### 1450 1451<sup>536</sup> **4.4 Incision rates**

1452  
1453  
1454<sup>537</sup> River incision rates have been calculated by comparing the vertical separation (m) and  
1455  
1456  
1457<sup>538</sup> the elapsed time (ka) between successive terrace strath surfaces. For this level of  
1458  
1459<sup>539</sup> analysis, we considered that strath formation and the deposition of the corresponding  
1460  
1461<sup>540</sup> alluvium are generally synchronous in time. The terrace sequences at Ainsa (kilometer  
1462  
1463<sup>541</sup> 50 from headwaters; upper valley reach) and at Albalate (kilometer 125 from  
1464  
1465  
1466<sup>542</sup> headwaters; lower valley reach) sectors (Fig. 6) were selected because of the extensive  
1467  
1468<sup>543</sup> presence of well-preserved terrace remnants in both areas (Figs. 3B, C, 4D, F).

1469  
1470<sup>544</sup> Differential mean heights, elapsed mean time and mean incision rates for the selected  
1471  
1472  
1473  
1474  
1475

1476  
1477  
1478  
1479<sup>545</sup> sets of coupled terraces are summarized in Table 5. Uncertainties in numerical dating  
1480  
1481<sup>546</sup> were also considered to present maximum and minimum fluvial incision rates (Table  
1482  
1483<sup>547</sup> 5).

1484  
1485  
1486<sup>548</sup> Considering mean incisions from the coupled successions Qt3-Qt7, Qt7-Qt9 and Qt9-  
1487  
1488<sup>549</sup> active channel, we proposed that a regional mean fluvial incision rate of 0.47 m ka<sup>-1</sup>  
1489  
1490  
1491<sup>550</sup> occurred during the Middle and Late Pleistocene. The spatial and temporal patterns of  
1492  
1493<sup>551</sup> river incision also show some singularities. Rates of fluvial incision decreased  
1494  
1495<sup>552</sup> downstream from Ainsa to Albalate; mean incision rates were 0.56 m ka<sup>-1</sup> at Ainsa and  
1496  
1497  
1498<sup>553</sup> 0.38 m ka<sup>-1</sup> at Albalate. Additionally, the mean incision rate obtained from the coupled  
1499  
1500<sup>554</sup> succession Qt3-Qt7 was 0.38 m ka<sup>-1</sup> at Ainsa and 0.20 m ka<sup>-1</sup> at Albalate (Table 5). For  
1501  
1502<sup>555</sup> the coupled succession Qt7-Qt9, values were 0.76 m ka<sup>-1</sup> and 0.61 m ka<sup>-1</sup>, respectively.  
1503  
1504  
1505<sup>556</sup> The coupled Qt9-active channel succession indicates incision of 0.54 m ka<sup>-1</sup> at Ainsa  
1506  
1507<sup>557</sup> and 0.33 m ka<sup>-1</sup> at Albalate. These results clearly indicate that incision rates were  
1508  
1509<sup>558</sup> higher on the upper reach relative to the lower reach over the considered time  
1510  
1511<sup>559</sup> intervals.

1512  
1513  
1514  
1515<sup>560</sup> The temporal pattern of variation in incision rates along the Cinca River valley reflects  
1516  
1517<sup>561</sup> important changes during the Middle and Late Pleistocene. These changes are well  
1518  
1519<sup>562</sup> observed in the Albalate sector, where the more complete sequence of terraces is  
1520  
1521<sup>563</sup> preserved (Table 5). The Middle Pleistocene coupled Qt3-Qt5 terraces reflects an  
1522  
1523  
1524<sup>564</sup> incision rate of 0.11 m ka<sup>-1</sup>. By comparison, the incision rate of 0.24 m ka<sup>-1</sup> was  
1525  
1526<sup>565</sup> considerably higher during the Middle-Late Pleistocene transition for the coupled Qt5-  
1527  
1528<sup>566</sup> Qt6 terraces. The Cinca River attained the highest incision rates during the Late  
1529  
1530<sup>567</sup> Pleistocene. Pairing the Qt6-Qt7 terraces gives an incision rate of 0.74 m ka<sup>-1</sup> and the  
1531  
1532  
1533  
1534

1535  
1536  
1537  
1538 568 coupled Qt7-Qt8 terraces yields the maximum calculated rate of 1.48 m ka<sup>-1</sup>. For the  
1539  
1540 569 coupled Qt8-Qt9 terraces and the Qt9-Active channel, incision rates were substantially  
1541  
1542 570 lower: 0.26 m ka<sup>-1</sup> and 0.33 m ka<sup>-1</sup>, respectively (Table 5; Fig. 8). Time-related trends in  
1543  
1544 571 incision rates along the Ainsa sector, where the number of couples of terraces is less,  
1545  
1546 572 were similar (Table 5; Fig. 8). As a consequence, the temporal incision pattern shows  
1547  
1548  
1549 573 very low rates over the Middle Pleistocene, a gradual increase until the beginning of  
1550  
1551 574 the Late Pleistocene (maximum rates at 60-50 ka) and then a gradual decrease to the  
1552  
1553 575 present.

1554  
1555  
1556 576 Additionally, taking into account the proposed paleomagnetic dates for Qt1 (Jaramillo  
1557  
1558  
1559 577 event, 999-1070 ka) and Qt2 (reversed period previous Jaramillo event, 780-999 ka) in  
1560  
1561 578 the Albalate sector (Table 1), we can tentatively estimate mean incision rates of 0.06 m  
1562  
1563 579 ka<sup>-1</sup> and 0.34 m ka<sup>-1</sup> for the coupled terraces of Qt2-Qt3 and Qt1-Qt2, respectively  
1564  
1565 580 (Table 5; Fig. 8).

## 1566 581 **5. Discussion**

1570  
1571  
1572 582 Landscape evolution and regional fluvial incision reflects an integration between uplift  
1573  
1574 583 and climate (e.g., Whipple and Tucker, 1999; Gibbard and Lewin, 2009; Wegmann and  
1575  
1576 584 Pazzaglia, 2009; Westaway et al., 2009; Stokes et al., 2012; Pazzaglia, 2013). Some  
1577  
1578  
1579 585 studies have defined the geodynamic state (e.g., Lewis et al., 2000; Cloetingh et al.,  
1580  
1581 586 2002; Garcia-Castellanos et al., 2003; Gunnell et al., 2008; Casas-Sainz and de Vicente,  
1582  
1583 587 2009; Fernández-Lozano et al., 2011) and the climate evolution based on fluvial  
1584  
1585  
1586 588 records (Fuller et al., 1998; Lewis et al., 2009; Benito et al. 2010; García-Ruiz et al.,  
1587  
1588 589 2013; Whitfield et al., 2013; Sancho et al., 2015) during the Quaternary in NE Spain.  
1589  
1590  
1591  
1592  
1593

1594  
1595  
1596  
1597 590 The results presented above provide an opportunity to better understand the factors  
1598  
1599 591 constraining regional and temporal fluvial incision patterns in the NE Iberian Peninsula.  
1600  
1601

### 1602 592 **5.1 Regional fluvial incision pattern**

1603  
1604

1605 593 The regional pattern of the Cinca River incision can be basically defined by (i) the well-  
1606  
1607  
1608 594 marked vertical separation between successive terrace straths, (ii) the near-parallel  
1609  
1610 595 terrace strath profiles, and (iii) the westward migration of the Cinca River through  
1611  
1612 596 time. The calculated mean river incision rate in the Cinca River valley (Pyrenees and  
1613  
1614 597 Ebro Basin) during the Middle and Late Pleistocene was  $0.47 \text{ m ka}^{-1}$ . This rate is similar  
1615  
1616  
1617 598 to channel incision rates of  $\leq 1 \text{ m ka}^{-1}$  for mountainous regions where commonly  
1618  
1619 599 paired and extensive terraces occur (Wegmann and Pazzaglia, 2009). A maximum  
1620  
1621 600 incision rate of  $0.98 \text{ m ka}^{-1}$  in the Miranda basin (Upper Ebro river valley), also within  
1622  
1623 601 the Pyrenees, has been indicated by Soria-Jáuregui et al. (2016). Although regional  
1624  
1625  
1626 602 data on river incision rates across the Iberian Peninsula are limited, the topographic  
1627  
1628 603 pattern of river incision in the Pyrenees and the Ebro Basin is clearly different than  
1629  
1630 604 those observed in the nearby Iberian Range (Giachetta et al., 2015) or in other  
1631  
1632 605 extensive Iberian Tertiary basins drained by rivers flowing into the Atlantic Ocean.  
1633  
1634  
1635 606 Mean fluvial incision rates of  $0.065 \text{ m ka}^{-1}$  from the terrace sequence of the Arlanzón  
1636  
1637 607 River (Duero Basin) have been reported by Moreno et al. (2012), and a figure of  $0.05 \text{ m}$   
1638  
1639 608  $\text{ka}^{-1}$  for terraces in different river valleys in the Central Tagus Basin has been roughly  
1640  
1641 609 estimated by Silva et al. (2013, 2016). Fluvial incision rates of  $0.07\text{-}1 \text{ m ka}^{-1}$  (Cunha et  
1642  
1643  
1644 610 al., 2005, 2008) and  $0.13\text{-}0.53 \text{ m ka}^{-1}$  (Martins et al., 2009) have been calculated from  
1645  
1646 611 terrace sequences in the Lower Tagus River basin.  
1647  
1648  
1649  
1650  
1651  
1652

1653  
1654  
1655 612 *5.1.1 Vertical separation between strath terraces*  
1656  
1657  
1658

1659 613 In the Cinca River valley, vertical separation between couples of adjacent terrace  
1660  
1661 614 straths ranged from approximately 10 to 50 m near Albalate (Table 5). Uplift must be  
1662  
1663 615 sufficiently high to produce well marked altitudinal separation between terraces  
1664  
1665 616 (Wang et al., 2015). He et al. (2015) obtained incision rates of 0.62-1.83 m ka<sup>-1</sup> for  
1666  
1667  
1668 617 terraces developed in rapidly uplifting mountainous areas (SE Tibetan Plateau), clearly  
1669  
1670 618 higher than in the Cinca River valley under post-tectonic conditions. Many studies have  
1671  
1672 619 demonstrated how long-term incision rates serve as a proxy for bedrock uplift rates  
1673  
1674 620 (Merritts et al., 1994; Bridgland, 2000; Pazzaglia and Brandon, 2001; Wegmann and  
1675  
1676  
1677 621 Pazzaglia, 2002; Bridgland and Westaway, 2008).

1678  
1679  
1680 622 There are three regional geodynamic mechanisms that likely explain the geomorphic  
1681  
1682 623 expression of the incision of the Cinca River. First, post-orogenic lithosphere uplift in  
1683  
1684 624 the northeastern Iberian margin could be at least partially attributed to isostatic  
1685  
1686  
1687 625 adjustment resulting from crustal thickening influenced by pre-existing faults (Casas-  
1688  
1689 626 Sainz and de Vicente, 2009; Fernández-Lozano et al., 2011).

1690  
1691  
1692 627 Second, lithosphere uplift could also be related to erosional unloading in the Pyrenees  
1693  
1694 628 and the Ebro Basin after the connection of the drainage system with the  
1695  
1696  
1697 629 Mediterranean Sea at the end of the Late Miocene (Coney et al., 1996; Vergés et al.,  
1698  
1699 630 1998; Waltham et al., 2000; Garcia-Castellanos et al., 2003; Gibson et al., 2007; Stange  
1700  
1701 631 et al., 2016; Garcia-Castellanos and Larrasoña, 2015). Erosional denudation has  
1702  
1703  
1704 632 prevailed for at least the last 10 Ma in the Central Pyrenees (Coney et al., 1996;  
1705  
1706 633 Fitzgerald et al., 1999; Garcia-Castellanos et al., 2003; Gibson et al., 2007) and  
1707  
1708  
1709  
1710  
1711

1712  
1713  
1714  
1715 634 thermochronologic (U-Th/He) data indicate uniformly low rates (0.2 mm/yr) (Gibson et  
1716  
1717 635 al., 2007). On the other hand, it should be noted that the thickness of sedimentary fill  
1718  
1719 636 in the north-central sector of the Ebro basin during the Late Oligocene and Early  
1720  
1721 637 Miocene exceeded 5,000 m and consequently caused important flexural load effects  
1722  
1723 638 on the lithosphere (Gaspar-Escribano et al., 2001). Considering the topography of the  
1724  
1725  
1726 639 youngest Tertiary rocks (Pérez-Rivarés et al., 2002) preserved in the Central Ebro Basin  
1727  
1728 640 (Monte Oscuro and San Caprasio, 812 m a.s.l.) and the altitude of the active Cinca  
1729  
1730 641 channel close to the confluence into the Ebro River (Mequinenza Reservoir, 80 m  
1731  
1732 642 a.s.l.), a denudation of 750 m must be considered as a minimum to explain the  
1733  
1734  
1735 643 erosional rebound. The flexural isostatic compensation of the eroded materials from  
1736  
1737 644 the Ebro basin is considered by Garcia-Castellanos and Larrasoña (2015) to be the  
1738  
1739 645 major force driving fluvial incision and topographic development.  
1740  
1741  
1742 646 A third factor that could also modulate Quaternary regional uplift required to develop  
1743  
1744  
1745 647 the terrace sequence of the Cinca River is the occurrence of a warm, buoyant  
1746  
1747 648 asthenosphere perhaps related to adjacent active crustal extension and volcanism in  
1748  
1749 649 northeastern Spain (Lewis et al., 2000). This is further supported by Janssen et al.  
1750  
1751  
1752 650 (1993) who presented a model of subsidence in the Valencia Trough and associated  
1753  
1754 651 uplift in the eastern Iberian margin during the Pliocene. Mantle dynamics during post-  
1755  
1756 652 orogenic stages may also account for the uplift in the Pyrenees and the Ebro southern  
1757  
1758 653 foreland basin (Stange et al., 2016). However, Garcia-Castellanos and Larrasoña  
1759  
1760  
1761 654 (2015) considered forces related to mantle flow to have a minor role in building the  
1762  
1763 655 post-tectonic topography of the Ebro basin.  
1764  
1765  
1766  
1767  
1768  
1769  
1770

1771  
1772  
1773  
1774 656 Finally, although numerical dates to establish correlations are very limited, the broadly  
1775  
1776 657 uniform altimetry of the staircase terrace sequences in the valleys of the main  
1777  
1778 658 tributaries flowing into the Ebro River from the Pyrenees (Noguera Ribagorzana, Cinca,  
1779  
1780 659 Alcanadre and Gállego rivers, from east to west) is noticeable (Gutiérrez and Peña,  
1781  
1782 660 1994).

### 1785 1786 661 5.1.2 Near-parallel strath profiles

1789 662 In addition to vertical separation between terrace straths of the Cinca River, near-  
1790  
1791 663 parallel concave-upward terrace profiles were also clearly demonstrated (Fig. 6).  
1792  
1793  
1794 664 Steady regional crustal uplift would drive uniform fluvial incision and invariant incision  
1795  
1796 665 rates, resulting in parallel terrace longitudinal profiles (Schlunegger and Hinderer,  
1797  
1798 666 2001; Pazzaglia, 2013). As a consequence, we postulate a trend to a uniform uplift rate  
1799  
1800 667 over the Pleistocene in NE Iberia.

1802  
1803  
1804 668 A weak trend upstream divergence of strath profiles was also observed. The upstream  
1805  
1806 669 divergence among Qt3, Qt7 and Qt9 profiles includes a decrease in terrace gradient  
1807  
1808 670 from Qt3 to Qt9 terraces (Fig. 6). The stream gradient controls both the stream-power  
1809  
1810 671 and the transport capacity (Hack, 1973) through flow velocity. On the other hand,  
1811  
1812  
1813 672 bedload movement by rolling is related to flow velocity near the streambed (Chorley et  
1814  
1815 673 al., 1984). As a consequence, gravel-size transport is directly related to channel  
1816  
1817 674 gradient. Considering the more representative strath terraces along the Cinca River  
1818  
1819  
1820 675 valley (Qt3, Qt7 and Qt9), the maximum grain size ( $D_{max}$ ) ( $34\pm 6$  cm,  $34\pm 9$  cm and  
1821  
1822 676  $29\pm 12$  cm, respectively) remained near-uniform (Fig. 5). Then, flow velocity during  
1823  
1824 677 deposition of the Qt3, Qt7 and Qt9 alluvium remained nearly uniform. Clast-size  
1825  
1826  
1827  
1828  
1829

averages of the entire set of terraces overlapped within uncertainties. A decrease in the maximum grain size ( $D_{max}$ ) along each terrace profile has also been observed (Fig. 5), which indicates that the hydraulic shear stress decreases proportionally to the gradient of the stream (Schumm, 1977; Larue, 2008; Pazzaglia, 2013).

The upstream divergence of terrace straths along the Cinca River indicates differential regional uplift as a primary driver of terrace formation rather than changes in fluvial erosivity and incision driven by cycles of climate transition (Whipple et al., 1999; Whipple and Tucker, 1999). Several mechanisms may be involved to explain the postulated differential regional uplift: (i) a reinforced uplift in response to a higher denudation rate affecting the Pyrenees as a function of topographic relief (Champagnac et al., 2008; Stange et al., 2016); (ii) an isostatic rebound of the Central Pyrenees related to lithospheric thickening (Zeyen and Fernández, 1994; Gunnel et al., 2008), supported by an important negative Bouguer anomaly associated with the Pyrenean building (Casas et al., 1997); and (iii) a flexural rebound related to removal of Pleistocene glaciers in the headwaters of the Cinca-Cinqueta valley (Belmonte, 2014).

### *5.1.3 Migration westward of the Cinca River*

The Cinca River has markedly migrated to the west during incision, based on the distribution of mapped terrace surfaces (Fig. 3B, C; Appendix 1). The maximum lateral westward displacement reached 7 km between Qt3 and Qt7 in the Albalate section of the lower Cinca River valley. Westward migration ceased from the Qt7 terrace ( $61 \pm 4$  ka). The observed arrangement of the terraces extends to the regional scale because it is common in the Pyrenean side of the central Ebro Basin, as has been shown in the

1889  
1890  
1891 700 Noguera Ribagorzana River valley (Peña-Monné, 1983; Sancho, 1988), to the east of  
1892  
1893  
1894 701 the Cinca River, in the Alcanadre River valley (Rodríguez, 1986; Calle et al., 2013), and  
1895  
1896 702 the Gállego River valley (Benito, 1989), to the west of the Cinca River.  
1897  
1898  
1899 703 Lateral migration can play an important role in the river incision rates because it  
1900  
1901 704 maintains an unconstrained width of the valley over time and, as a consequence, the  
1902  
1903  
1904 705 obtained river incision rates could be comparable. Fluvial incision into bedrock is  
1905  
1906 706 basically proportional to the stream power and inversely proportional to the channel  
1907  
1908 707 width (Howard et al., 1994; Sklar and Dietrich, 1998; Brocard and van der Beek, 2006).  
1909  
1910 708 Terrace treads of the Qt1 to Qt7 terraces consist of wide aggradational surfaces (Figs.  
1911  
1912 709 3B, C, 4; Appendix 1). For example, the Qt3 valley section is approximately a minimum  
1913  
1914  
1915 710 of 5.5 km wide at Barbastro and the Qt7 valley width reaches a minimum of 4.5 km at  
1916  
1917 711 Santa Lecina. Subsequent to formation of the Qt7 terrace, the river valley becomes  
1918  
1919 712 narrower and the available width to accommodate subsequent terraces decreases  
1920  
1921 713 (Qt8 and Qt9) to a maximum of 2 km between Monzón and Fraga. Considering the  
1922  
1923 714 uniform lithology of the geological bedrock (Schanz and Montgomery, 2016), the  
1924  
1925 715 higher erosivity from Qt7 to Qt9 (the pair Qt7-Qt8 yields a rate of  $1.48 \text{ m ka}^{-1}$ ),  
1926  
1927 716 therefore, could be, at least partially, related to restrictions imposed by valley width.  
1928  
1929  
1930  
1931  
1932 717 Channel migration and the related asymmetry of Pleistocene terraces may also be  
1933  
1934 718 controlled by the regional westward tilt of Oligocene-Miocene bedrock in the Ebro  
1935  
1936 719 basin. Strata dip gently westward ( $5^\circ$  maximum) along the western margin of the Cinca  
1937  
1938 720 River valley (Sancho, 1988). This regional tilting requires an uplift mechanism more  
1939  
1940  
1941 721 active in eastern Iberia, with tilting related to the uplift of the rift shoulder (including  
1942  
1943 722 the eastern Pyrenees, the Catalan Coastal Ranges and the adjacent Ebro Basin)  
1944  
1945  
1946  
1947

(Janssen et al., 1993; Casas-Sainz and de Vicente, 2009) accompanying the opening of the western Mediterranean margin during the Neogene (Roca and Desegaulx, 1992; Coney et al., 1996; Lewis et al., 2000). The uniform altimetry of the sequences of terraces in the main Pyrenean tributaries of the Ebro River, from east to west, however, suggests a cessation of differential uplift in the Mediterranean shoulder from at least the Mid Pleistocene. As a consequence, increased eastern uplift plays an indirect role in the westward migration of the Cinca River through the tilting bedrock.

## ***5.2 Changes in incision rates over the last 1 Ma***

Analysis of incision rates indicates that non-uniform river incision in the Cinca River valley has occurred over the last 1 Ma (Table 5; Fig. 8). Temporal changes in fluvial incision rates are particularly well established in the lower reach of the valley where the terrace sequence is preserved. Changes in river incision rates over time can be linked to changes in uplift rates (He et al., 2015; Ruszkiczay-Rüdiger et al., 2016) and/or climate driven changes in erosivity (e.g., Whipple et al., 1999; Schlunegger and Hinderer, 2001; Hartshorn et al., 2002; Zaprowski et al., 2005; Yang et al., 2011).

Using currently available data, there is no evidence of variability in the tectonic uplift rate of NE Iberia during the Mid-Late Pleistocene (Casas-Sainz and de Vicente, 2009; Fernández-Lozano et al., 2011); however, strong variability in climate has been well established, particularly during the Penultimate and the Last Glacial cycles at regional scale (Lewis et al., 2009; Sancho et al., 2015). Lewis et al. (2009) linked fluvial aggradation phases during the Mid-Late Pleistocene in the Cinca River valley with enhanced periods of glacier outwash that produced high discharges of water and

2007  
2008  
2009 745 sediment yield down-stream along the valley. Therefore, a close correlation was  
2010  
2011 established between alluvial deposition and cold stages: Qt5 correlates to MIS6, Qt6 to  
2012 746  
2013 the MIS5b-5c transition, Qt7 to MIS4, Qt8 to the H5 event and Qt9 to the Younger  
2014 747  
2015 Dryas period (Lewis et al., 2009). Periods of higher fluvial incision would be likely  
2016 748  
2017 during interstadial stages with a lower sediment supply and greater water discharge  
2018 749  
2019 activated by retreating glaciers. There is a broad agreement that correlates valley  
2020 750  
2021 aggradation to cold climates and river incision to transitional and warm climates (e.g.,  
2022 751  
2023 Chorley et al., 1984; Fuller et al., 1998; Vandenberghe and Maddy, 2001; Macklin et al.,  
2024 752  
2025 2002; Pan et al., 2003; Vandenberghe, 2003; Gao et al., 2008; Wegmann and Pazzaglia,  
2026 753  
2027 2009).  
2028 754  
2029  
2030  
2031  
2032  
2033 755 Regional incision also reflects cycles of variable glacial meltwater discharge over time  
2034  
2035 756 as a function of the extension and retreat of the Cinca and Cinqueta valley glaciers. For  
2036  
2037 757 example, the last maximum glacier advance in the Central Pyrenees was at 60-70 ka  
2038  
2039 (MIS4) (Sancho et al., 2003; Lewis et al., 2009) and correlates well with the Qt7 terrace  
2040 758  
2041 (Lewis et al., 2009), the most important geomorphological marker along the valley. The  
2042 759  
2043 Cinca-Cinqueta glacier system reached a length of 25 km at this time. Subsequent  
2044 760  
2045 glacier retreat would produce increased runoff that, in turn, would accelerate fluvial  
2046 761  
2047 downcutting resulting in higher rates of river incision (Dethier, 2001). As result, the  
2048 762  
2049 highest expected fluvial incision rates would occur during the timing of the couple Qt7-  
2050 763  
2051 Qt8 (from 61±4 ka to 47±4 ka) following the last maximum glacier extension. In fact,  
2052 764  
2053 this is the case; the incision rate was 1.48 m ka<sup>-1</sup> in the lower reach of the Cinca River  
2054 765  
2055 valley (Albalate sector). Nonetheless, the decrease in valley width after Qt7 formation  
2056 766  
2057  
2058  
2059  
2060  
2061  
2062  
2063  
2064  
2065

2066  
2067  
2068  
2069  
2070  
2071  
2072  
2073  
2074  
2075  
2076  
2077  
2078  
2079  
2080  
2081  
2082  
2083  
2084  
2085  
2086  
2087  
2088  
2089  
2090  
2091  
2092  
2093  
2094  
2095  
2096  
2097  
2098  
2099  
2100  
2101  
2102  
2103  
2104  
2105  
2106  
2107  
2108  
2109  
2110  
2111  
2112  
2113  
2114  
2115  
2116  
2117  
2118  
2119  
2120  
2121  
2122  
2123  
2124

767 must also be considered to explain this high incision rate, as has been previously  
768 indicated.

769 The incision rates obtained between Qt6 (97±16 ka) and Qt7 (61±4 ka) formation (0.74  
770 m ka<sup>-1</sup>) and between Qt9 and the active channel (last 11±1 ka) (0.33 m ka<sup>-1</sup>) are also  
771 remarkable. Significantly lower incision rates were deduced during the Mid-  
772 Pleistocene (e.g., 0.11 m ka<sup>-1</sup> between Qt3 and Qt5 in the Albalate sector), resulting  
773 from less intense glacial pulses and/or higher valley width maintained as a  
774 consequence of the migration westward of the Cinca River. Our results do not well  
775 match the acceleration in river incision during the Mid-Pleistocene Revolution at the  
776 global scale (Bridgland and Westaway, 2008). Regardless, the general temporal pattern  
777 in the lower reach of the Cinca River valley (Albalate sector) can be extrapolated to the  
778 upper reach (Ainsa sector).

779 Finally, agreement between denudation and isostatic rebound must also be considered  
780 (Garcia-Castellanos and Lasarrosa, 2015). The increase in fluvial entrenchment would  
781 involve a lowering of the regional drainage and an increased denudation between Qt6  
782 (97±16 ka) and Qt8 (47±4 ka), which in turn implies a higher erosional isostatic uplift  
783 during this period demonstrating a positive feedback loop (Finnegan et al., 2008;  
784 Westaway et al., 2009; Schlunegger et al., 2011).

## 6. Conclusions

785 Incision rates derived from the regional distribution of a well-preserved sequence of  
786 staircase terraces along 170 km in the Cinca River valley have been developed for the  
787 last 1 Ma in the Central Pyrenees and the adjacent Ebro basin (NE Iberia). The

2125  
2126  
2127  
2128 789  
2129  
2130 790  
2131  
2132 791  
2133  
2134 792  
2135  
2136 793  
2137  
2138  
2139 794  
2140  
2141 795  
2142  
2143  
2144 796  
2145  
2146 797  
2147  
2148  
2149 798  
2150  
2151 799  
2152  
2153 800  
2154  
2155 801  
2156  
2157  
2158 802  
2159  
2160 803  
2161  
2162  
2163 804  
2164  
2165  
2166 805  
2167  
2168 806  
2169  
2170 807  
2171  
2172 808  
2173  
2174  
2175 809  
2176  
2177 810  
2178  
2179 811  
2180  
2181  
2182  
2183

sequence is composed of ten well separated terraces (from Qt1 to Qt10) formed under post-orogenic geodynamics and glacial/ interglacial climate conditions. Formation of this extensive paired cyclic terrace sequence was climatically controlled and required a significant regional uplift. Combined results from terrace mapping, height of terrace straths and profiles, and numerical ages of the alluvium overlying terrace straths allow analysis of the spatial and temporal river incision patterns and provides several interpretation of mechanisms involved:

1) Considering coupled successions of the more extensive terraces (Qt3-Qt7, Qt7-Qt9 and Qt9-active channel), the mean fluvial incision rate along the Cinca River during the Middle and Late Pleistocene was approximately around  $0.47 \text{ m ka}^{-1}$ . This incision rate was slightly greater in the upper reach of the valley (Ainsa sector) ( $0.56 \text{ m ka}^{-1}$ ) than in the lower reach (Albalate sector) ( $0.38 \text{ m ka}^{-1}$ ). In addition, the highest incision rate ( $1.48 \text{ m ka}^{-1}$ ) in the lower reach of the valley occurred during Qt7-Qt8 terrace formation (61-47 ka) and the lowest rate ( $0.11 \text{ m ka}^{-1}$ ) occurred during Qt3-Qt5 terrace formation (401-178 ka).

2) The spatial distribution of incision rates showed a near-uniform pattern of fluvial down-cutting along the Cinca River valley. Nearly parallel terrace profiles were driven by a near-uniform regional uplift activated by (i) tectonic uplift related to lithospheric thickening and (ii) isostatic rebound in response to regional denudation unloading, after the connection of the Ebro Basin with the Mediterranean Sea. Subtle upstream divergence of strath profiles appears to be governed by a differential increased uplift in the upper mountainous reach of the valley (Axial Pyrenees) rather than by a decrease in climate-driven erosivity with time.

2184  
2185  
2186 812 3) Temporal incision rates show a non-uniform time pattern throughout the last 1 Ma.  
2187  
2188

2189 813 The highest incision rate ( $1.48 \text{ m ka}^{-1}$ ) occurred during Qt7-Qt8 terrace formation (61-  
2190  
2191 814 47 ka). This highest rate appears to be related to a combination of (i) the high glacial  
2192  
2193 815 meltwater discharge after the last maximum advance of the Pyrenean Cinca-Cinqueta  
2194  
2195 816 glacier system and (ii) by the deactivation of migration westward of the Cinca River,  
2196  
2197  
2198 817 favouring a lower width of the valley. Currently, the Cinca River is not in equilibrium  
2199  
2200 818 and modern incision continues.  
2201  
2202

2203 819 Incision rates calculated in the Ebro Basin draining to the Mediterranean Sea are much  
2204  
2205 820 higher than rates for the Iberian rivers flowing into the Atlantic Ocean. Undoubtedly,  
2206  
2207  
2208 821 the post-tectonic geodynamic setting of NE Iberia, the denudation triggered after the  
2209  
2210 822 exorheism of the Ebro basin and the Pleistocene glacier evolution in the Pyrenees play  
2211  
2212 823 a determinant role in explaining this difference in landscape evolution at the Iberian  
2213  
2214 824 scale.  
2215  
2216  
2217

2218 825 Additional regional studies of staircase terrace sequences are necessary to validate the  
2219  
2220 826 proposed spatial and temporal patterns and to confirm the combined effect of uplift  
2221  
2222 827 and climate on fluvial incision rates and the landscape evolution of NE Iberia.  
2223  
2224  
2225

## 2226 828 **7. Acknowledgments**

2227  
2228  
2229 829 This paper is a tribute to Dr. Claudia J. Lewis, who died prematurely when we were  
2230  
2231 830 developing the manuscript. At the picture, Claudia guiding a field-trip to the Cinca  
2232  
2233 831 River Valley included in the program of the V Spanish Geological Congress (2004). The  
2234  
2235  
2236 832 paper collects much of the hard work performed cooperatively between 1998 and  
2237  
2238 833 2012. Research was funded by grants from the National Geographic Society, the  
2239  
2240  
2241  
2242

2243  
2244  
2245 834 National Science Foundation (EAR-0088714), U.S. Army Research Office grants  
2246  
2247  
2248 835 DAAD19-03-1-0159 and W911NF-09-1-0256, the Spanish Ministry of Education, and a  
2249  
2250 836 Fulbright Senior Scholar grant to C. Lewis. We thank the Institute of Geophysics and  
2251  
2252 837 Planetary Physics and Laboratory Directed Research and Development (LDRD) at Los  
2253  
2254 838 Alamos National Laboratory for additional funding. The Desert Research Institute  
2255  
2256  
2257 839 provided GPS equipment. Laboratory soil analyses were carried out at the Desert  
2258  
2259 840 Research Institute. We thank John Geissman, Bet Beamud and Miguel Garcés for use of  
2260  
2261 841 the paleomagnetic labs at the University of New Mexico (Albuquerque) and the  
2262  
2263 842 Institute of Earth Sciences “Jaume Almera” CSIC-UB (Barcelona, Spain). We thank  
2264  
2265  
2266 843 Marta Lopez for combining all of our data into a Geographic Information System. This  
2267  
2268 844 study is a contribution of the PALEOQ Research Group (Aragon Government and  
2269  
2270 845 European Social Fund) and IUCA (University of Zaragoza). Authors thank two  
2271  
2272 846 anonymous reviewers for their comments that helped improve the manuscript. Thanks  
2273  
2274  
2275 847 are also due to the Editor Prof. Andy Plater for the final refinement of the manuscript.  
2276  
2277

## 2278 848 **References**

2279  
2280  
2281 849 Antón, L., Rodés, A., De Vicente, G., Pallàs, R, Garcia-Castellanos, D., Stuart, F.M.,  
2282  
2283  
2284 850 Braucher, R. and Bourlès, D. (2012). Quantification of fluvial incision in the Duero Basin  
2285  
2286 851 (NW Iberia) from longitudinal profile analysis and terrestrial cosmogenic nuclide  
2287  
2288 852 concentrations. *Geomorphology*, 165-166, 50-61.  
2289  
2290  
2291  
2292 853 Bailey, R.C. and Halls, H.C. (1984). Estimate of confidence in paleomagnetic directions  
2293  
2294 854 derived from mixed remagnetization circle and direct observational data. *Journal of*  
2295  
2296 855 *Geophysics*, 54, 174-182.  
2297  
2298  
2299  
2300  
2301

2302  
2303  
2304 856 Barnolas, A., Gil-Peña, I. and Martín-Alfageme, S. (2009). Mapa Geológico de Pirineos a  
2305  
2306 escala 1:400.000. IGME-BRGM.  
2307 857  
2308  
2309  
2310 858 Belmonte, A. (2014). Geomorfología del Macizo de Cotiella (Pirineo oscense):  
2311  
2312 859 Cartografía, evolución paleoambiental y dinámica actual. PhD thesis, University of  
2313  
2314 860 Zaragoza, 580 p.  
2315  
2316  
2317  
2318 861 Beltrán, A. (1985). Historia de Aragón, vol. II. Guara Editorial, 183 p. Zaragoza.  
2319  
2320  
2321 862 Benito, G. (1989). Geomorfología de la Cuenca Baja del río Gállego. PhD thesis,  
2322  
2323 863 University of Zaragoza, 764 p.  
2324  
2325  
2326  
2327 864 Benito, G., Sancho, C., Peña, J.L., Machado, M.J. and Rhodes, E.J. (2010). Large-scale  
2328  
2329 865 karst subsidence and accelerated fluvial aggradation during MIS6 in NE Spain: climatic  
2330  
2331 866 and paleohydrological implications. Quaternary Science Reviews, 29, 2694-2704.  
2332  
2333  
2334  
2335 867 Birkeland, P.W. (1999). Soils and Geomorphology. Oxford University Press, New York.  
2336  
2337 868 430 p.  
2338  
2339  
2340 869 Bridgland, D.R. (2000). River terrace systems in north-west Europe: an archive of  
2341  
2342 870 environmental change, uplift and early human occupation. Quaternary Science  
2343  
2344  
2345 871 Reviews, 19, 1293-1303.  
2346  
2347  
2348 872 Bridgland, D. and Westaway, R. (2008). Climatically controlled river terrace staircases:  
2349  
2350 873 A worldwide Quaternary phenomenon. Geomorphology , 98, 285-315.  
2351  
2352  
2353  
2354 874 Brocard, G.Y. and van der Beek, P.A. (2006). Influence of incision rate, rock strength,  
2355  
2356 875 and bedload supply on bedrock river gradients and valley-flat widths: field-based  
2357  
2358  
2359  
2360

2361  
2362  
2363 876 evidence and calibrations from western Alpine rivers (southeast France). In Willet, S.D.,  
2364  
2365 Hovious, N., Brandon, M.T. and Fisher, D.M. (Eds.). Tectonics, Climate and Landscape  
2366 877  
2367 Evolution. Geological Society of America, Special Paper 398, 101-126.  
2368 878  
2369  
2370  
2371 879 Bull, W.B. (1991). Geomorphic Response to Climatic Change. Oxford University Press,  
2372  
2373 880 326 p. New York.  
2374  
2375  
2376  
2377 881 Burbank, D.W. and Anderson, R.S. (2001). Tectonic Geomorphology. Blackwell, 274  
2378  
2379 882 Malden.  
2380  
2381  
2382 883 Calle, M., Sancho, C., Peña, J.L., Cunha, P., Oliva-Urcia, B. and Pueyo, E. (2013). La  
2383  
2384 884 secuencia de terrazas cuaternarias del río Alcanadre (provincia de Huesca):  
2385  
2386 caracterización y consideraciones paleoambientales. Cuadernos de Investigación  
2387 885 Geográfica, 39, 159-178.  
2388  
2389 886 Casas, A., Kearey, P., Rivero, L. and Adam, C.R. (1997). Gravity anomaly map of the  
2390  
2391  
2392 887 Pyrenean region and a comparison of the deep geological structure of the western and  
2393  
2394 888 eastern Pyrenees. Earth and Planetary Science Letters, 150, 65-78.  
2395  
2396  
2397 889 Casas-Sainz, A.M. and de Vicente, G. (2009). On the tectonic origin of Iberian  
2398  
2399  
2400 890 topography. Tectonophysics, 474, 214-235.  
2401  
2402  
2403 891  
2404  
2405  
2406 892 Champagnac, J.D., van der Beek, P., Diraison, G. and Dauphin, S. (2008). Flexural  
2407  
2408 893 isostatic response of the Alps to increased Quaternary erosion recorded by foreland  
2409  
2410 894 basin remnants, SE France. Terra Nova, 20, 213-220.  
2411  
2412  
2413  
2414 895 Chorley, R.J., Schumm, S.A. and Sugden, D.E. (1984). Geomorphology. Methuen, 605 p.  
2415  
2416 896 London.  
2417  
2418  
2419

2420  
2421  
2422  
2423 897 Cloetingh, S. and Willett, S.D. (2013). TOPO-EUROPE: Understanding of the coupling  
2424 between the deep Earth and continental topography. *Tectonophysics*, 602, 1-14.  
2425 898  
2426  
2427  
2428 899 Cloetingh, S., Burov, E., Beekman, F., Andeweg, B., Andriessen, P.A.M., Garcia-  
2429  
2430 900 Castellanos, D., de Vicente, G. and Vegas, R. (2002). Lithospheric folding in Iberia.  
2431  
2432 Tectonics, 21, 5-1-5-26.  
2433 901  
2434  
2435  
2436 902 Coney, P.J., Muñoz, J.A., McClay, K.R. and Evenchick, C.A. (1996). Syntectonic burial  
2437 and post-tectonic exhumation of the southern Pyrenees foreland fold-and-thrust belt.  
2438 903  
2439  
2440 904 Journal of the Geological Society, London, 153, 9-16.  
2441  
2442  
2443  
2444 905 Costa, E., Garcés, M., López-Blanco, M., Beamud, E., Gómez-Paccard, M. and  
2445  
2446 906 Larrasoaña, J.C. (2010). Closing and continentalization of the South Pyrenean foreland  
2447 basin (NE Spain): magnetochronological constraints. *Basin Research*, 26, 904-917.  
2448 907  
2449  
2450  
2451 908 Cunha, P.P., Martins, A.A., Daveau, S., Friend, P. (2005). Tectonic control of the Tejo  
2452 river fluvial incision during the late Cenozoic, in Ródão-central Portugal (Atlantic  
2453 Iberian border). *Geomorphology*, 64, 271-298.  
2454 909  
2455  
2456 910  
2457  
2458  
2459 911 Cunha, P.P., Martins, A.A., Huot, S., Murray, A.S. and Raposo, L. (2008). Dating the Tejo  
2460 river lower terraces in the Ródão area (Portugal) to assess the role of tectonics and  
2461 uplift. *Geomorphology*, 102, 43-54.  
2462 912  
2463  
2464 913  
2465  
2466  
2467 914 Cunha, P.P., Almeida, N., Aubry, T., Martins, A.A., Murray, S.A., Buylaert, J.P., Sohbaty,  
2468 R., Raposo, L. and Rocha, L. (2012). Records of human occupation from Pleistocene  
2469 river terrace and aeolian sediments in the Arneiro depression (Lower Tejo River,  
2470 central eastern Portugal). *Geomorphology*, 165-166, 78-90.  
2471 916  
2472  
2473  
2474 917  
2475  
2476  
2477  
2478

2479  
2480  
2481 918 Dethier, D.P. (2001). Pleistocene incision rates in the western United States calibrated  
2482 using lava Creek B tephra. *Geology*, 29, 783-786.  
2483  
2484 919  
2485  
2486  
2487 920 Dubar, M. and Semah, F. (1986). Paleomagnetic data bearing on the age of high terrace  
2488 deposits (Durance Sequence) in Alpine valleys of southeastern France. *Quaternary  
2489 Research*, 25, 387-391.  
2490  
2491 922  
2492  
2493  
2494  
2495 923 Duval, M., Sancho, C., Calle, M., Guilarte, V. and Peña-Monné, J.L. (2015). On the  
2496 potential of the ESR dating method applied to optically bleached quartz grains in  
2497 924 sedimentary fluvial environments: some examples from the Early Pleistocene terraces  
2498 of the Alcanadre river (Ebro basin, Spain). *Quaternary Geochronology*, 29, 58-69.  
2499 925  
2500  
2501 926  
2502  
2503  
2504  
2505 927 Fernández-Lozano, J., Sokoutis, D., Willingshofer, E., Muñoz-Martín, A., De Vicente, G.  
2506 and Cloetingh, S., (2011). Análisis integrado de la topografía y anomalías gravimétricas  
2507 928 en la Península Ibérica: nuevas metodologías en modelación análoga. *Revista de la  
2508 Sociedad Geológica de España*, 24, 153-171.  
2509 929  
2510  
2511 930  
2512  
2513  
2514  
2515 931 Finnegan, N.J., Hallet, B., Montgomery, D.R., Zeitler, P.K., Stone, J.O., Anders, A.M. and  
2516 Yuping, L. (2008). Coupling of rock uplift and river incision in the Namche Barwa-Gyala  
2517 932 Peri massif, Tibet. *Geological Society of America Bulletin*, 120, 142-155.  
2518  
2519 933  
2520  
2521  
2522  
2523 934 Fisher, R. (1953). Dispersion on a sphere. *Proceedings of the Royal Society of London.  
2524 Series A. Mathematical and Physical Sciences*, 217, 295-305.  
2525 935  
2526  
2527  
2528 936 Fitzgerald, P.G., Muñoz, J.A., Coney, P.J. and Baldwin, S.L. (1999). Asymmetric  
2529 exhumation across the Pyrenean orogen: implications for the tectonic evolution of a  
2530 collisional orogen. *Earth and Planetary Science Letters*, 173, 157-170.  
2531 937  
2532  
2533 938  
2534  
2535  
2536  
2537

2538  
2539  
2540  
2541 939 Fuller, I.C., Macklin, M.G., Lewin, J., Passmore, D.G. and Wintle, A.G. (1998). River  
2542 response to high-frequency climate oscillations in southern Europe over the past 200  
2543 940 k.y. *Geology*, 26, 275-278.  
2544  
2545 941  
2546  
2547  
2548 942 Gao, H., Liu, X., Pan, B., Wang, Y., Yu, Y. and Li, J. (2008). Stream response to  
2549 Quaternary tectonic and climatic change: Evidence from the upper Weihe River,  
2550 943 central China. *Quaternary International*, 186, 123-131.  
2551  
2552  
2553 944  
2554  
2555  
2556 945 Garcia-Castellanos, D., Vergés, J., Gaspar-Escribano, J. and Cloetingh, S. (2003).  
2557 Interplay between tectonics, climate, and fluvial transport during the Cenozoic  
2558 946 evolution of the Ebro Basin (NE Iberia). *Journal of Geophysical Research*, 108, 2347,  
2559 doi:10.1029/2002JB002073.  
2560  
2561 947  
2562  
2563 948  
2564  
2565  
2566 949 Garcia-Castellanos, D. and Larrasoaña, J.C. (2015). Quantifying the post-tectonic  
2567 topographic evolution of closed basins: The Ebro basin (northeast Iberia). *Geology*,  
2568 950 43, 663-666.  
2569  
2570  
2571 951  
2572  
2573  
2574 952 García-Ruiz, J.M., Martí-Bono, C., Peña-Monné, J.L., Sancho, C., Rhodes, E.J., Valero-  
2575 Garcés, B., González-Sampériz, P. and Moreno, A. (2013). Glacial and fluvial deposits in  
2576 953 the Aragón Valley, central-western Pyrenees: chronology of the Pyrenean late  
2577 Pleistocene glaciers. *Geografiska Annaler: Series A, Physical Geography*, 95, 15-32.  
2578 954  
2579  
2580  
2581 955  
2582  
2583  
2584 956 Gaspar-Escribano, J. M., van Wees, J. D., ter Voorde, M., Cloetingh, S., Roca, E.,  
2585 Cabrera, L., Muñoz, J. A., Ziegler, P. A. and Garcia-Castellanos, D. (2001). Three-  
2586 957 dimensional flexural modelling of the Ebro Basin (NE Iberia). *Geophysical Journal  
2587 International*, 145, 349-367.  
2588 958  
2589  
2590  
2591 959  
2592  
2593  
2594  
2595  
2596

2597  
2598  
2599 960 Giachetta, E., Molin, P., Scotti, V.N. and Faccena, C. (2015). Plio-Quaternary uplift of  
2600  
2601 the Iberian Chanin (central-eastern Spain) from landscape evolution experiments and  
2602 961  
2603 river profile modeling. *Geomorphology*, 246, 48-67.  
2604 962  
2605  
2606  
2607 963 Gibbard, P. and Cohen, K.M. (2008). Global chronostratigraphical correlation table for  
2608  
2609 the last 2.7 million years. *Episodes*, 31, 243-247.  
2610 964  
2611  
2612  
2613 965 Gibbard, P.L. and Lewin, J. (2009). River incision and terrace formation in the late  
2614  
2615 Cenozoic of Europe. *Tectonophysics* 474, 41-55.  
2616  
2617  
2618 967 Gibson, M., Sinclair, H.D., Lynn, G.J. and Stuart, F.M. (2007). Late- to post-orogenic  
2619  
2620 exhumation of the Central Pyrenees revealed through combined thermochronological  
2621 968  
2622 data and modeling. *Basin Research*, 19, 323-334.  
2623 969  
2624  
2625  
2626 970 Gil Garbi, H, 2017. Los depósitos cuaternarios en el sector central de la Cuenca del  
2627  
2628 Ebro: Arquitectura sedimentaria, paleokarst, su interacción con la sedimentación y  
2629 971  
2630 cronología. PhD thesis, University of Zaragoza, 354 p.  
2631 972  
2632  
2633  
2634 973 Gil, H., Luzón, A., Soriano, M.A., Casado, I., Pérez, A., Yuste, A., Pueyo, E.L. and Pocoví,  
2635  
2636 A. (2013). Stratigraphic architecture of alluvial-aeolian systems developed on active  
2637 974  
2638 karst terrains: an Early Pleistocene example from the Ebro Basin (NE Spain).  
2639 975  
2640  
2641 976 *Sedimentary Geology*, 296, 122-141.  
2642  
2643  
2644 977 Gile, L.H., Hawley, J.H. and Grossman, R.B. (1981). Soils and geomorphology in the  
2645  
2646 basin and range area of Southern New Mexico-guidebook to the desert project. New  
2647 978  
2648 Mexico Bureau of Mines and Mineral Resources, Socorro, NM. Memoir 39, 222 p.  
2649 979  
2650  
2651  
2652  
2653  
2654  
2655

2656  
2657  
2658  
2659 980 Gunnell, Y., Zeyen, H. and Calvet, M. (2008). Geophysical evidence of a missing  
2660 lithospheric root beneath the Eastern Pyrenees: Consequences for post-orogenic uplift  
2661 981 and associated geomorphic signatures. *Earth and Planetary Science Letters*, 276, 302-  
2662 313.  
2663 982  
2664  
2665 983  
2666  
2667  
2668 984 Gutiérrez, M. and Peña, J.L. (1994). Depresión del Ebro. In Gutiérrez, M. (Ed.).  
2669 Geomorfología de España, 305-349. Ed. Rueda. Madrid.  
2670  
2671 985  
2672  
2673  
2674 986 Hack, J.T. (1973). Stream-profile analysis and stream-gradient index. *Journal Research*  
2675 U.S. Geological Survey, 1, 421-429.  
2676 987  
2677  
2678  
2679  
2680 988 Harden, J.W. (1982). A quantitative index of soil development from field descriptions:  
2681 examples from a soil chronosequence in central California. *Geoderma*, 28, 1-28.  
2682 989  
2683  
2684  
2685 990 Harden, J.W. and Taylor, E.M. (1983). A quantitative comparison of soil development in  
2686 four climatic regimes. *Quaternary Research*, 20, 342-359.  
2687 991  
2688  
2689  
2690  
2691 992 Hartshorn, K., Hovius, N., Dade, W.B. and Slingerland, R.L. (2002). Climate-driven  
2692 bedrock incision in an active mountain belt. *Science*, 297, 2036-2038.  
2693 993  
2694  
2695  
2696 994 He, Z., Zhang, X., Bao, S., Qiao, Y., Sheng, Y., Liu, X., He, X., Yang, X., Zhao, J., Liu, R. and  
2697 Lu, C. (2015). Multiple climatic cycles imprinted on regional uplift-controlled fluvial  
2698 terraces in the lower Yalong River and Anning River, SE Tibetan Plateau.  
2699 995  
2700  
2701 996  
2702  
2703 997  
2704  
2705  
2706 998  
2707 Howard, A.D., Dietrich, W.E. and Seidl, M.A. (1994). Modeling fluvial erosion on  
2708 regional to continental scales. *Journal of Geophysical Research* 99 (B7), 13,971-13,986.  
2709 999  
2710  
2711  
2712  
2713  
2714

2715  
2716  
2717  
1000 Jacobson, R.B., Elston, D. P. and Heaton, J.W. (1988). Stratigraphy and magnetic  
2718  
2719 polarity of the high terrace remnants in the upper Ohio and Monongahela rivers in  
2720 1001  
2721 West Virginia, Pennsylvania, and Ohio. *Quaternary Research*, 29, 216-232.  
2722 1002  
2723  
2724  
2725 1003 Janssen, M.E., Torné, M., Cloetingh, S. and Banda, E. (1993). Pliocene uplift of the  
2726  
2727 eastern Iberian margin: inferences from quantitative modelling of the Valencia Trough.  
2728 1004  
2729 Earth and Planetary Science Letters, 119, 585-597.  
2730 1005  
2731  
2732  
2733 1006 Kirschvink, J.L. (1980). The least-squares line and plane and the analysis of  
2734  
2735 palaeomagnetic data. *Geophysical Journal of the Royal Astronomical Society*, 62, 699-  
2736 1007  
2737 718.  
2738 1008  
2739  
2740  
2741 1009 Larue, J.P. (2008). Tectonic influence on the Quaternary drainage evolution on the  
2742  
2743 northwestern margin of the French Central Massif: the Cruese valley example.  
2744 1010  
2745 Geomorphology, 93, 398-420.  
2746 1011  
2747  
2748  
2749 1012 Lewis, C., McDonald, E., Sancho, C., Peña, J.L. and Rhodes, E. (2009). Climatic  
2750  
2751 implications of correlated Upper Pleistocene glacial and fluvial deposits on the Cinca  
2752 1013  
2753 and Gállego Rivers (NE Spain) based on OSL dating and soil stratigraphy. *Global and*  
2754 1014  
2755 *Planetary Change*, 67, 141-152.  
2756 1015  
2757  
2758  
2759 1016 Lewis, C.J., Vergés, J. and Marzo, M. (2000). High mountains in a zone of extended  
2760  
2761 crust: Insights into the Neogene-Quaternary topographic development of northeastern  
2762 1017  
2763 Iberia. *Tectonics*, 19, 86-102.  
2764 1018  
2765  
2766  
2767 1019 Li, J.J., Fang, X.M., van der Voo, R., Zhu, J.J., Mac Niocaill, C., Ono, Y., Pan, B.T., Zhong,  
2768  
2769 W., Wang, J.L., Sasaki, T., Zhang, Y.T, Cao, J.X., Kang, S.C. and Wang, J.M. (1997).  
2770 1020  
2771  
2772  
2773

2774  
2775  
2776  
1021 Magnetostratigraphic dating of river terraces: Rapid and intermittent incision by the  
2777  
2778  
1022 Yellow River of the northeastern margin of the Tibetan Plateau during the Quaternary.  
2779  
2780  
2781023 Journal of Geophysical Research, 102, 10121-10132.  
2782  
2783  
2784  
1024 Lucha, P., Gutiérrez, F. and Guerrero, J. (2008). Environmental problems and geological  
2785  
2786  
1025 implications derived from evaporite dissolution in the Barbastro salt anticline (NE  
2787  
2788  
1026 Spain). Environmental Geology, 53, 1045-1055.  
2789  
2790  
2791  
2792  
1027 Macklin, M.G., Fuller, I.C., Lewin, J., Maas, G.S., Passmore, D.G., Rose, J., Woodward,  
2793  
2794  
1028 J.C., Black, S., Hamlin, R.H.B. and Rowan, J.S. (2002). Correlation of fluvial sequences in  
2795  
2796  
1029 the Mediterranean basin over the last 200 ka and their relationship to climate change.  
2797  
2798  
1030 Quaternary Science Reviews, 21, 1633-1641.  
2800  
2801  
2802  
1031 Martínez-Peña, M. and Casas-Sainz, A. (2003). Cretaceous-Tertiary tectonic inversion  
2803  
2804  
1032 of the Cotiella Basin (southern Pyrenees, Spain). International Journal of Earth  
2805  
2806  
1033 Sciences, 92, 99-113.  
2807  
2808  
2809  
2810  
1034 Martínez-Peña, B., Casas-Sainz, A. and Millán-Garrido, H. (1995). Palaeostresses  
2811  
2812  
1035 associated with thrust sheet emplacement and related holding folding in the southern  
2813  
2814  
1036 central Pyrennes, Huesca, Spain. Journal of the Geological Society, London, 152, 353-  
2815  
2816  
1037 364.  
2817  
2818  
2819  
2820  
1038 Martins, A.A., Cunha, P.P., Huot, S., Murray, A.S. and Buylaert, J.P. (2009).  
2821  
2822  
1039 Geomorphological correlation of the tectonically displaced Tejo River terraces  
2823  
2824  
1040 (Gavião-Chamusca area, central Portugal) supported by luminescence dating.  
2825  
2826  
1041 Quaternary International, 199, 75-91.  
2827  
2828  
2829  
2830  
2831  
2832

2833  
2834  
2835  
1042 Martins, A.A., Cunha, P.P., Buylaert, J.P., Huot, S., Murray, A.S., Dinis, P., Stokes, M.  
2836  
2837  
1043 (2010). K-feldspar IRSL dating of a Pleistocene river terrace sequence of the Lower Tejo  
2838  
2839  
1044 River (Portugal, western Iberia). *Quaternary Geochronology*, 5, 176-180.  
2840  
2841  
2842  
2843  
1045 McDonald, E.V., Reneau, S.L. and Gardner, J.N. (1996). Soil-forming processes on the  
2844  
2845  
1046 Pajarito Plateau: Investigation of a soil chronosequence in Rendija Canyon. In: Goff, F.,  
2846  
2847  
1047 Kues, B.S., Rogers, M.A., McFadden, L.D. and Gardner, J.N. (Eds.), *New Mexico*  
2848  
2849  
1048 *Geological Society Guidebook, 47th Conference. Socorro, New Mexico, USA*, p. 375-  
2850  
2851  
1049 382.  
2852  
2853  
2854  
2855  
1050 Merritts, J., Vicent, R. and Wohl, E. (1994). Long river profiles, tectonism and eustasy: a  
2856  
2857  
1051 guide to interpreting fluvial terraces. *Journal of Geophysical Research* 99 (B7), 14031-  
2858  
2859  
1052 14050.  
2860  
2861  
2862  
2863  
1053 Miall, A.D. (1978). Lithofacies types and vertical profile models in braided river  
2864  
2865  
1054 deposits: a summary. In: Miall, A.D. (Ed.). *Fluvial sedimentology. Canadian Society of*  
2866  
2867  
1055 *Petroleum Geologists, Memoir 5*, 597-604.  
2868  
2869  
2870  
2871  
1056 Moreno, D., Falguères, C., Pérez-González, A., Duval, M., Voinchet, P., Benito-Calvo, A.,  
2872  
2873  
1057 Ortega, A.I., Bahain, J.J., Sala, R., Carbonell, E., Bermúdez de Castro, J.M. and Arsuaga,  
2874  
2875  
1058 J.L. (2012). ESR chronology of alluvial deposits in the Arlanzón valley (Atapuerca,  
2876  
2877  
1059 Spain): Contemporaneity with Atapuerca Gran Dolina site. *Quaternary Geochronology*,  
2878  
2879  
1060 10, 418-423.  
2880  
2881  
2882  
2883  
1061 Muñoz, J.A. (2002). The Pyrenees. In Gibbons, W. and Moreno, M.T. (Eds.). *The*  
2884  
2885  
1062 *Geology of Spain*, 370-385. Geological Society, London.  
2886  
2887  
2888  
2889  
2890  
2891

2892  
2893  
2894  
1063 Muñoz, A., Arenas, C., González, A., Luzón, A., Pardo, G., Pérez, A. and Villena, J.  
2895  
2896  
1064 (2002). Ebro basin (northeastern Spain). In Gibbons, W. and Moreno, M.T. (Eds.). The  
2897  
2898  
1065 Geology of Spain, 301-309. Geological Society, London.  
2899  
2900  
2901  
2902  
1066 Pan, B.T., Burbank, D., Wang, Y.X., Wu, G.J., Li, J.J. and Guan, Q.Y. (2003). A 900 ka  
2903  
2904  
1067 record of strath terrace formation during glacial-interglacial transitions in northwest  
2905  
2906  
1068 China. *Geology*, 31, 957-960.  
2907  
2908  
2909  
1069 Pazzaglia, F.J. (2013). Fluvial Terraces. In Wohl, E. (Ed.). *Treatise of Geomorphology*,  
2910  
2911  
1070 Volume 9, 379-412. Elsevier.  
2912  
2913  
2914  
2915  
1071 Pazzaglia, F.J. and Brandon, M.T. (2001). A fluvial record of rock uplift and shortening  
2916  
2917  
1072 across the Cascadia forearc high. *American Journal of Science*, 301, 385-431.  
2918  
2919  
2920  
2921  
1073 Peña-Monné, J.L. (1983). La Conca de Tremp y Sierras Prepirenaicas comprendidas  
2922  
2923  
1074 entre los ríos Segre y Noguera Ribagorzana: estudio geomorfológico. Instituto de  
2924  
2925  
1075 Estudios Ilerdenses, 373 p., Lleida.  
2926  
2927  
2928  
2929  
1076 Peña-Monné, J.L. (1994). Cordillera Pirenaica. In Gutiérrez, M. (Ed.). *Geomorfología de*  
2930  
2931  
1077 *España*, 159-225. Rueda, Madrid.  
2932  
2933  
2934  
1078 Pérez-Rivarés, J., Garcés, M., Arenas, C. and Pardo, G. (2002). Magnetocronología de la  
2935  
2936  
1079 sucesión Miocena de la Sierra de Alcubierre (sector central de la Cuenca del Ebro).  
2937  
2938  
1080 *Revista Sociedad Geológica de España*, 15, 3-4.  
2939  
2940  
2941  
2942  
1081 Pevzner, M.A. (1970). Paleomagnetic studies of Pliocene-Quaternary deposits of  
2943  
2944  
1082 Pridniestrovie. *Palaeogeography, Palaeoclimatology, Palaeoecology*, 8, 215-219.  
2945  
2946  
2947  
2948  
2949  
2950

2951  
2952  
2953  
1083 Pueyo, E.L., Garcés, M., Mauritsch, H.J., Lewis, C., Scholger, R., Sancho, C., Molina, R.,  
2954  
2955  
1084 Schnepf, E., Larrasoña, J.C., Parés, J.M., Pocoví, A., Muñoz, A., Valero, B., Millán, H.,  
2956  
2957  
1085 Laplana, C., Oliva, B. and González, P. (2006). Sampling, transportation and magnetic-  
2958  
2959  
1086 free consolidation of extremely soft sediments for paleomagnetic purposes: a  
2960  
2961  
1087 successful "recipe". In Calvo, M., Garcés, M., Gomes, C., Larrasoña, J.C., Pueyo, E. and  
2962  
2963  
1088 Villalaín, J.J. (Eds). MAGIBER I: Paleomagnetismo en la Península Ibérica, 121-128.  
2964  
2965  
1089 Universidad de Burgos, ISBN: 84-96394-35-2.  
2966  
2967  
2968  
2969  
1090 Puigdefábregas, C. and Souquet, P. (1986). Tecto-sedimentary cycles and depositional  
2970  
2971  
1091 sequences of the Mesozoic and Tertiary from the Pyrenees. In Banda, E. and Wickham,  
2972  
2973  
1092 S.M. (Eds.). The Geological Evolution of the Pyrenees, Tectonophysics, 129, 173-203.  
2974  
2975  
2976  
2977  
1093 Ramón, M.J., Pueyo, E.L., Oliva-Urcia, B. and Larrasoña, J.C. (2017). Virtual Directions  
2978  
2979  
1094 in Paleomagnetism: A Global and Rapid Approach to Evaluate the NRM Components.  
2980  
2981  
1095 Frontiers of Earth Science, 5, 1-14.  
2982  
2983  
2984  
2985  
1096 Roca, E. and Desegaulx, P. (1992). Analysis of the geological evolution and vertical  
2986  
2987  
1097 movements in the València trough area, western Mediterranean. Marine and  
2988  
2989  
1098 Petroleum Geology, 9, 167-185.  
2990  
2991  
2992  
2993  
1099 Rodríguez, J. (1986). Geomorfología de las Sierras Exteriores oscenses y su  
2994  
2995  
1100 piedemonte. Instituto de Estudios Altoaragoneses, Huesca, 172 p.  
2996  
2997  
2998  
2999  
1101 Ruskiczay-Rüdiger, Z., Braucher, R., Novothny, A., Csillag, G., Fodor, L., Molnár, G.,  
3000  
3001  
1102 Madarász, B. and ASTER Team (2016). Tectonic and climatic control on terrace  
3002  
3003  
1103 formation: Coupling in situ produced <sup>10</sup>Be depth profiles and luminescence approach,  
3004  
3005  
1104 Danube River, Hungary, Central Europe. Quaternary Science Reviews, 131, 127-147.  
3006  
3007  
3008  
3009

3010  
3011  
3012  
1105 Sancho, C. (1988). Geomorfología de la cuenca baja del río Cinca. PhD thesis, University  
3013  
3014  
1106 of Zaragoza, 743 p.  
3015  
3016  
3017  
3018  
1107 Sancho, C. (1989). Deformaciones asociadas a la actividad diapírica cuaternaria del  
3019  
3020  
1108 Anticlinal de Barbastro (provincia de Huesca). Cuaternario y Geomorfología, 3, 35-43.  
3021  
3022  
3023  
1109 Sancho, C., Calle, M., Peña-Monné, J.L., Duval, M., Oliva-Urcia, B., Pueyo, E.L., Benito,  
3024  
3025  
1110 G. and Moreno, A. (2016). Dating the earliest Pleistocene alluvial terrace of the  
3026  
3027  
1111 Alcanadre River: Insights on the landscape evolution of the Ebro Basin (NE Spain).  
3028  
3029  
1112 Quaternary International, 407, 86-95.  
3030  
3031  
3032  
3033  
1113 Sancho, C., Peña, J.L., Lewis, C., McDonald, E. and Rhodes, E. (2003). Preliminary dating  
3034  
3035  
1114 of glacial and fluvial deposits in the Cinca River Valley (NE Spain): chronological  
3036  
3037  
1115 evidences for the Glacial Maximum in the Pyrenees?. In Ruiz, M.B., Dorado, M.,  
3038  
3039  
1116 Valdeolmillos, A., Gil, M.J., Bardají, T., Bustamante, I. and Martínez, I. (Eds.).  
3040  
3041  
1117 Quaternary climatic changes and environmental crises in the Mediterranean region,  
3042  
3043  
1118 169-173. Universidad de Alcalá-Ministerio de Ciencia y Tecnología-INQUA.  
3044  
3045  
3046  
3047  
1119 Sancho, C., Arenas, C., Vázquez-Urbez, M., Pardo, G., Lozano, M.V., Peña-Monné, J.L.,  
3048  
3049  
1120 Hellstrom, J., Ortiz, J.E., Osácar, M.C., Auqué, L. and Torres, T. (2015). Climatic  
3050  
3051  
1121 implications of the Quaternary fluvial tufa record in the NE Iberian Peninsula over the  
3052  
3053  
1122 last 500 ka. Quaternary Research, 84, 398-414.  
3054  
3055  
3056  
3057  
1123 Santisteban, J. I. and Schulte, L. (2007). Fluvial networks of the Iberian Peninsula: a  
3058  
3059  
1124 chronological framework. Quaternary Science Reviews, 26, 2738-2757.  
3060  
3061  
3062  
3063  
3064  
3065  
3066  
3067  
3068

3069  
3070  
3071 1125 Schanz, S.A. and Montgomery, D.R. (2016). Lithologic controls on valley width and  
3072  
3073 strath terrace formation. *Geomorphology*, 258, 58-68.  
3074 1126  
3075  
3076  
3077 1127 Scheepers, P.J.J. and Zijdeveld, J.D.A. (1992). Stacking in Paleomagnetism: Application  
3078  
3079 1128 to marine sediments with weak NRM, *Geophysical Research Letters*, 19, 1519-1522.  
3080  
3081  
3082 1129 Schlunegger, F. and Hinderer, M. (2001). Crustal uplift in the Alps: why the drainage  
3083  
3084 pattern matters. *Terra Nova*, 13, 425-432.  
3085 1130  
3086  
3087  
3088 1131 Schlunegger, F., Norton, K.P. and Zeilinger, G. (2011). Climatic forcing on channel  
3089  
3090 1132 profiles in the Eastern Cordillera on the Coroico region, Bolivia. *The Journal of Geology*,  
3091  
3092 1133 119, 97-107.  
3093  
3094  
3095  
3096 1134 Schumm, S.A. (1977). *The fluvial system*. John Wiley & Sons, 338 p. New York.  
3097  
3098  
3099 1135 Scotti, V.N., Molin, P., Faccenna, C., Soligo, M. and Casas-Sainz, A. (2014). The influence  
3100  
3101 1136 of surface and tectonic processes on landscape evolution of the Iberian Chain (Spain):  
3102  
3103 1137 quantitative geomorphological analysis and geochronology. *Geomorphology*, 206, 37-  
3104  
3105 1138 57.  
3106  
3107  
3108  
3109 1139 Sklar, L. and Dietrich, W.E. (1998). River longitudinal profiles and bedrock incision  
3110  
3111 1140 models: stream power and the influence of sediment supply. In: Tinkler, K.J. and Wohl,  
3112  
3113 E.E. (Eds.). *Rivers Over Rock: Fluvial Processes in Bedrock Channels*. *Geophysical*  
3114 1141 *Monograph*, 107. American Geophysical Union, 237-260. Washington D.C.  
3115  
3116 1142  
3117  
3118  
3119 1143 Silva, P.G., Roquero, E., López-Recio, M., Huerta, P. and Tapias, F. (2013). Statistical  
3120  
3121 1144 approach to the chronosequence of fluvial terraces in the Tagus and Duero basins  
3122  
3123  
3124  
3125  
3126  
3127

3128  
3129  
3130  
3131 1145 (Central Spain). In: Baena, R., Fernández, J.J. and Guerrero, I. (Eds.). El Cuaternario  
3132 Ibérico: Investigación en el S. XXI, 29-33. Sevilla.  
3133 1146  
3134  
3135  
3136 1147 Silva, P.G., Roquero, E., López-Recio, M., Huerta, P. and Martínez-Graña, A.M. (2016).  
3137  
3138 1148 Chronology of fluvial terrace sequences for large Atlantic rivers in the Iberian Peninsula  
3139  
3140 (Upper Tagus and Duero drainage basins, Central Spain). Quaternary Science Reviews  
3141  
3142 doi.org/10.1016/j.quascirev.2016.05.027.  
3143 1150  
3144  
3145  
3146 1151 Singer, B.S. (2014). A Quaternary geomagnetic instability time scale. Quaternary  
3147  
3148 1152 Geochronology, 21, 29-52.  
3149  
3150  
3151  
3152 1153 Soria-Jáuregui, A., González-Amuchástegui, M.J., Mauz, B. and Lang, A. (2016).  
3153  
3154 1154 Dynamics of Mediterranean late Quaternary fluvial activity: An example from the River  
3155  
3156 1155 Ebro (north Iberian Peninsula). Geomorphology, 268, 110-122.  
3157  
3158  
3159 1156 Stange, K.M., van Balen, R., Vandenberghe, J., Peña, J.L. and Sancho, C. (2013). External  
3160  
3161 controls on Quaternary fluvial incision and terrace formation at the Segre River,  
3162 1157  
3163 Southern Pyrenees. Tectonophysics, 602, 316-331.  
3164 1158  
3165  
3166  
3167 1159 Stange, K.M., van Balen, R.T., Garcia-Castellanos, D., Cloetingh, S. (2016). Numerical  
3168  
3169 modelling of Quaternary terrace staircase formation in the Ebro foreland basin,  
3170 1160  
3171 southern Pyrenees, NE Iberia. Basin Research, 28, 124-146.  
3172 1161  
3173  
3174  
3175 1162 Starkel, L. (2003). Climatically controlled terraces in uplifting mountain areas.  
3176  
3177 Quaternary Science Reviews, 22, 2189-2198.  
3178 1163  
3179  
3180  
3181 1164 Stokes, M., Cunha, P.P. and Martins, A. (2012). Techniques for analysing Late Cenozoic  
3182  
3183 1165 river terrace sequences. Geomorphology, 165, 1-6.  
3184  
3185  
3186

3187  
3188  
3189  
3190 1166 U.S. Soil Survey Staff (1993). Examination and description of soils. Soil Conservation  
3191 Service. Soil survey manual. U.S. Department of Agriculture Handbook 18. Washington,  
3192 1167  
3193 D.C., USA, Chapter 3.  
3194 1168  
3195  
3196  
3197 1169 Vandenberghe, J. (2003). Climate forcing of fluvial system development: an evolution  
3198 of ideas. Quaternary Science Reviews, 22, 2053-2060.  
3199 1170  
3200  
3201  
3202  
3203 1171 Vandenberghe, J. and Maddy, D. (2001). The response of river systems to climate  
3204 change. Quaternary International, 79, 1-3.  
3205 1172  
3206  
3207  
3208 1173 Vergés, J., Marzo, M., Santaèulària, T., Serra-Kiel, J., Burbank, D. W., Muñoz, J. A. and  
3209 Giménez-Montsant, J. (1998). Quantified vertical motions and tectonic evolution of the  
3210 SE Pyrenean foreland basin. In: Masclé, A., Puigdefàbregas, C., Luterbacher, H.P. and  
3211 1174 Fernández, M. (Eds.). Cenozoic Foreland Basins of Western Europe, London, Geological  
3212 Society Special Publications, 134, p. 107-134.  
3213 1175  
3214  
3215 1176  
3216  
3217 1177  
3218  
3219  
3220  
3221 1178 Viveen, W., Schoorl, J.M., Veldkamp, A. and van Balen, R.T. (2014). Modelling the  
3222 impact of regional uplift and local tectonics on fluvial terrace preservation.  
3223 1179  
3224 Geomorphology, 210, 119-135.  
3225 1180  
3226  
3227  
3228 1181 Waltham, D.C., Docherty, C., Taberner, C. (2000). Decoupled flexure in the South  
3229 Pyrenean foreland. J. Geophys. Res., 105, 16,329-16,340.  
3230  
3231 1182  
3232  
3233  
3234 1183 Wang, X., Vandenberghe, J., Shuangwen, Y., Van Balen, R. and Lu, H. (2015). Climate-  
3235 dependent fluvial architecture and processes on a suborbital timescale in areas of  
3236 1184 rapid tectonic uplift: An example from the NE Tibetan Plateau. Global and Planetary  
3237 Change, 133, 318-329.  
3238  
3239 1185  
3240  
3241 1186  
3242  
3243  
3244  
3245

3246  
3247  
3248  
3249 1187 Wegmann, K.W. and Pazzaglia, F.J. (2009). Late Quaternary fluvial terraces of the  
3250 Romagna and Marche Apennines, Italy: Climatic, lithologic, and tectonic controls on  
3251 1188  
3252 terrace genesis in an active orogen. *Quaternary Science Reviews*, 28, 137-165.  
3253 1189  
3254  
3255  
3256 1190 Westaway, R., Bridgland, D.R., Sinha, R. and Demir, T. (2009). Fluvial sequences as  
3257 evidence for landscape and climatic evolution in the Late Cenozoic: a synthesis of data  
3258 1191  
3259 from IGCP 518. *Global and Planetary Change*, 68, 237-253.  
3260 1192  
3261  
3262  
3263  
3264 1193 Whipple, K. and Tucker, G. (1999). Dynamics of the stream-power river incision model:  
3265 Implications for height limits of mountain ranges, landscape response timescales, and  
3266 1194  
3267 research needs. *Journal of Geophysical Research*, 104, 17661-17674.  
3268 1195  
3269  
3270  
3271  
3272 1196 Whipple, K.X., Kirby, E. and Brocklehurst, S.H. (1999). Geomorphic limits to climate-  
3273 induced increases in topographic relief. *Nature*, 401, 39-43.  
3274 1197  
3275  
3276  
3277 1198 Whitfield, R.G., Macklin, M.G., Brewer, P.A., Lang, A., Mau, B. and Whitfield (née  
3278 Maher), E. (2013). The nature, timing and controls of the Quaternary development of  
3279 1199  
3280 the Rio Bergantes, Ebro basin, northeast Spain. *Geomorphology*, 196, 106-121.  
3281 1200  
3282  
3283  
3284  
3285 1201 Willet, S.D., Hovius, N., Brandon, M.T. and Fischer, D.M. (2006). Introduction. In Willet,  
3286 S.D., Hovius, N., Brandon, M.T. and Fischer, D.M. (eds.). *Tectonic, climate and  
3287 1202  
3288 landscape evolution*. The Geological Society of America, 398, vii-xi.  
3289 1203  
3290  
3291  
3292  
3293 1204 Yang, G., Zhang, X., Tina, M., Brierley, G., Chen, A., Ping, Y., Ge, Z., Ni, Z. and Yang, Z.  
3294 (2011). Alluvial terrace systems in Zhangjiajie of northwest Hunan, China: Implications  
3295 1205  
3296 for climate change, tectonic uplift and geomorphic evolution. *Quaternary  
3297 1206  
3298 International*, 233, 27-39.  
3299 1207  
3300  
3301  
3302  
3303  
3304

3305  
3306  
3307  
3308 1208 Zaprowski, B.J., Pazzaglia, F.J. and Evenson, E.B. (2005). Climatic influences on profile  
3309 concavity and river incision. *Journal of Geophysical Research*, 110, F03004,  
3310 1209  
3311 doi:10.1029/2004JF000138.  
3312 1210  
3313  
3314

3315 1211 Zeyen, H. and Fernández, M. (1994). Integrated lithospheric modeling combining  
3316 thermal, gravity, and local isostasy analysis: application to the NE Spanish Geotransect.  
3317 1212  
3318 *Journal of Geophysical Research*, 99, 18089-18102.  
3319 1213  
3320 1214

### 3321 **Figure captions**

3322  
3323 1214  
3324  
3325  
3326 1215 Figure 1. Location of the Cinca River drainage basin and the Ebro Basin in NE Iberia.  
3327

3328  
3329  
3330 1216 Figure 2. Geological setting of the Cinca River Valley in NE Iberia (A) and geological  
3331 mapping of the bedrock (adapted from Barnolas et al., 2009) (B).  
3332 1217  
3333  
3334

3335 1218 Figure 3. Distribution of terraces along the Cinca River valley (A). Detailed  
3336 geomorphological maps and cross-sections of terraces in the Ainsa (B) and Albalate (C)  
3337 1219  
3338 sectors.  
3339 1220  
3340

3341  
3342  
3343 1221 Figure 4. Field photographs of terraces in the Cinca River valley: alluvial cover of the  
3344 terrace Qt7 overlaying Eocene marls near Ainsa (A) and Miocene clays and sandstones  
3345 1222  
3346 near Almudáfar (B); deposits of terrace Qt7 made of massive and cross-stratified  
3347 1223  
3348 gravels near Albalate (C); preserved staircase terrace sequences in the Ainsa (D),  
3349 1224  
3350  
3351  
3352 1225 Monzón (E) and Binaced (F) sectors.  
3353  
3354

3355 1226 Figure 5. Grain size trends for Cinca River terrace deposits (Qt3, Qt7, Qt9) decreasing  
3356 downstream.  
3357 1227  
3358  
3359  
3360  
3361  
3362  
3363

3364  
3365  
3366  
3367  
3368  
3369  
3370  
3371  
3372  
3373  
3374  
3375  
3376  
3377  
3378  
3379  
3380  
3381  
3382  
3383  
3384  
3385  
3386  
3387  
3388  
3389  
3390  
3391  
3392  
3393  
3394  
3395  
3396  
3397  
3398  
3399  
3400  
3401  
3402  
3403  
3404  
3405  
3406  
3407  
3408  
3409  
3410  
3411  
3412  
3413  
3414  
3415  
3416  
3417  
3418  
3419  
3420  
3421  
3422

Figure 6. Longitudinal profiles of the Cinca River terraces and the active channel.

General parallel profiles with a subtle trend to divergence upstream are observed.

Figure 7. Paleomagnetic analysis. Natural remanent magnetisation of the Cinca

Terraces (A), orthogonal demagnetisation diagrams of selected samples (B) and paleomagnetic means values in the studied terraces (C).

Figure 8. Fluvial incision rates in the Cinca River valley from successive preserved strath

terraces at the upper reach (Ainsa sector) and at the lower reach (Albalate sector) of

the valley. Spatial and temporal differences are clearly identified. Paleomagnetic

timescale and marine isotope stages (adapted from Gibbard and Cohen, 2008) are

included.

### **Table captions**

Table 1. Terraces, numerical dates and heights at the Albalate and Ainsa sectors of the Cinca River valley.

Table 2. Summary of relative degrees of soil development on the Cinca River terrace surfaces and estimated ages.

Table 3. OSL dates from terraces in the the Cinca River valley (adapted from Lewis et al., 2009).

Table 4. Paleomagnetic data. Location and UTM coordinates (T30). n/N;

considered/analysed samples. Pol: Polarity. Dec/inc: magnetic declination and

inclination and the Fisher (1954) statistical parameters ( $a_{95}$  and K).

3423  
3424  
3425  
3426  
3427  
3428  
3429  
3430  
3431  
3432  
3433  
3434  
3435  
3436  
3437  
3438  
3439  
3440  
3441  
3442  
3443  
3444  
3445  
3446  
3447  
3448  
3449  
3450  
3451  
3452  
3453  
3454  
3455  
3456  
3457  
3458  
3459  
3460  
3461  
3462  
3463  
3464  
3465  
3466  
3467  
3468  
3469  
3470  
3471  
3472  
3473  
3474  
3475  
3476  
3477  
3478  
3479  
3480  
3481

Table 5. Fluvial incision rates calculated from coupled preserved terraces in the Cinca River valley. Comparison of incision rates at the Ainsa and Albalate sectors is established. Temporal variations of incision rates at the Albalate sector are also evidenced.

### **Appendix captions**

Appendix 1. Detailed geological map (including strath terraces) of the Cinca River valley. GPS measurements of elevation of terrace straths and active channel points are also indicated.

Appendix 2. Cinca River terrace strath data measurements and observations. UTM coordinates (latitude and longitude), elevation, substrate lithology (abbreviations: gyp, gypsum; ls, limestone; sst, sandstone), alluvium thickness (m), maximum grain size (Dmax), location and distance from headwaters are indicated. UTM coordinates and strath heights were obtained from a differentially corrected GPS accurate to 1 cm. Measurements from the headwaters of the river were obtained from topographic maps 1:25,000 in scale.



Fig. 4

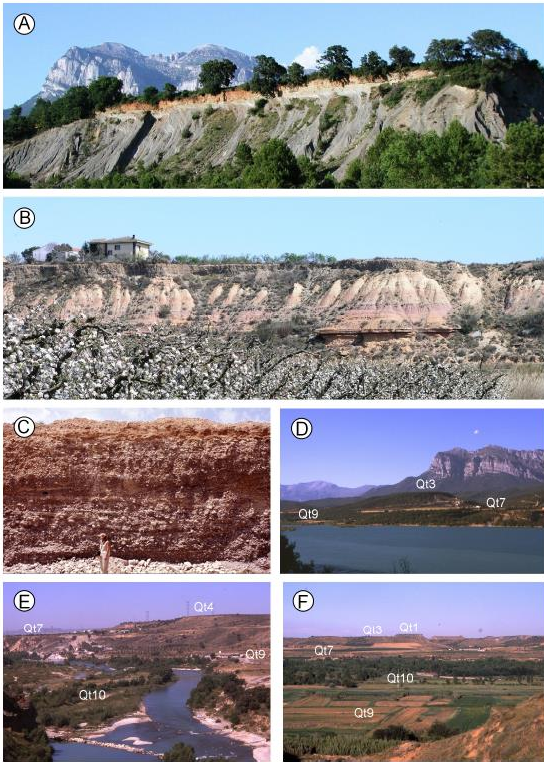


Fig. 7 below

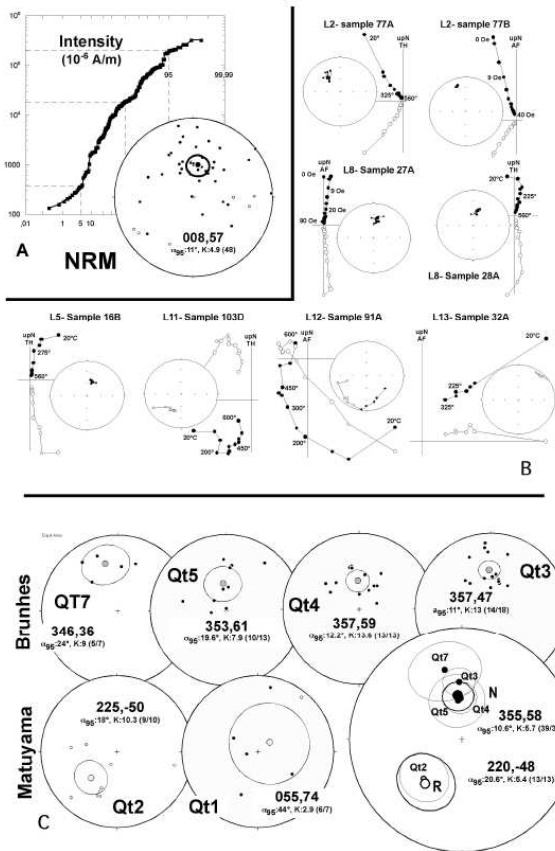


Fig. 5

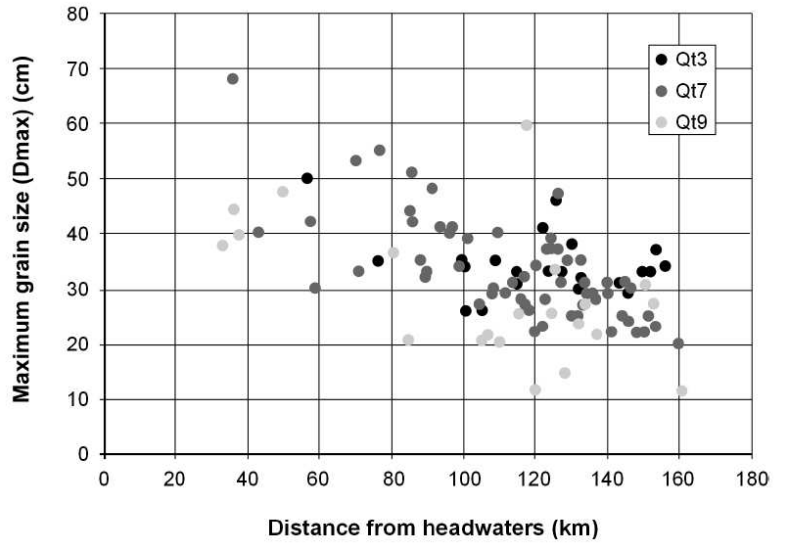


Fig. 6

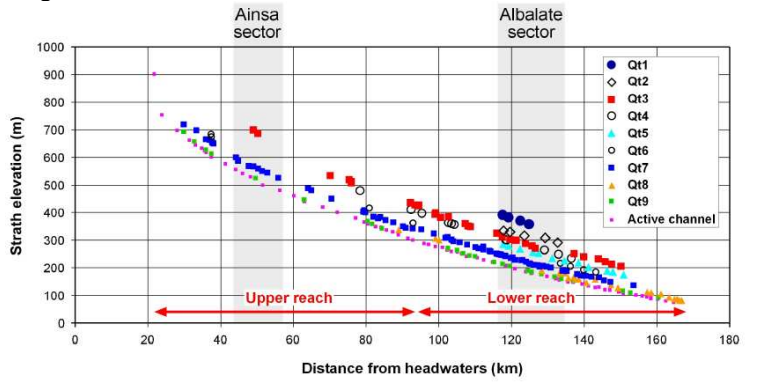
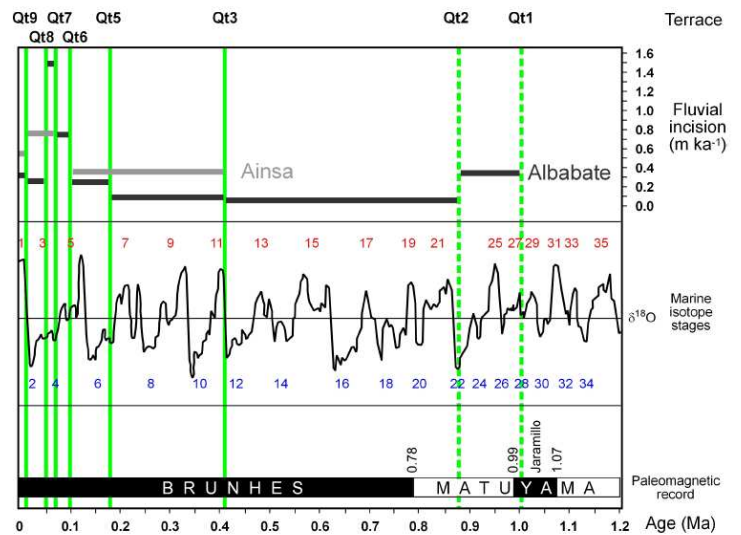


Fig. 8



# Appendix 1

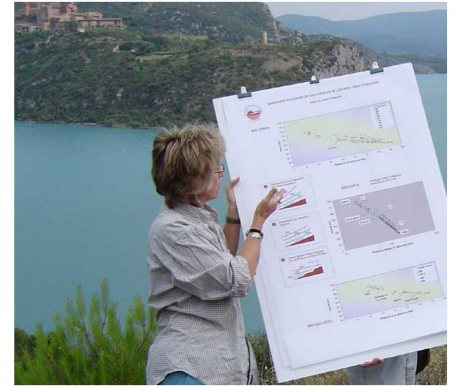


Table 1. Terraces, numerical dates and heights at the Albalate and Ainsa sectors of the Cinca River valley.

Terrace	Age (Ky)	Height (m)	
		Ainsa sector	Albalate sector
Qt1	999-1070 <sup>c</sup>	-	182.1
Qt2	780-999 <sup>c</sup>	-	132.5
Qt3	401±117 <sup>b</sup>	172.5	103.5
Qt4	-	-	91.3
Qt5	178 ± 21 <sup>a</sup>	-	79.9
Qt6	97±16 <sup>a</sup>	-	60.4
Qt7	61 ± 4 <sup>a</sup>	44.2	33.9
Qt8	47 ± 4 <sup>a</sup>	-	13.1
Qt9	11 ± 1 <sup>a</sup>	6.0	3.6

<sup>a</sup> Numerical age from Optical Stimulated Luminescence (Lewis et al., 2009)

<sup>b</sup> Age derived from soil chronofunction used in Lewis et al. (2009)

<sup>c</sup> Tentative age from paleomagnetic data



Table 2. Summary of relative degrees of soil development on the Cinca River terrace surfaces and estimated ages.

Terrace	PDI Value Range (number of soils) <sup>1</sup>	Soil Age <sup>2</sup>	Source of Age <sup>3</sup>	MAX B Horizon Type <sup>4</sup>	MAX Carbonate Stage Morphology <sup>5</sup>
<b>Albalate Sector</b>					
Qt9	14.7-18.1 (2)	11±1	OSL	Bk-Bwk	I+
Qt8	23.2-24.7 (2)	47±4	OSL	Bk-Btk	I-II
Qt7	27.0-33.3 (5)	61±4	OSL	Btk-Bkm	II-III
Qt6	43.2 (1)	97±16	OSL	Btk	III+
Qt5	45.1-59.9 (3)	178±21	OSL	Bk-Bkm	III+-IV+
Qt3 <sup>6</sup>	61.4-80.6 (5)	401±117	PDI	Bt-Bk-Bkm	IV-V+
<b>Ainsa Sector</b>					
Qt9	39.3 (1)	11±1	OSL	Btk	I
Qt7	64.4-67.9 (2)	61±4	OSL	Bt-Btk	I
Qt3	105.1 (1)	-	-	Bt	none

<sup>1</sup> Profile Development Index value and number of soils described shown in ( ). Minimum and maximum PDI values show when more than 2 soils

<sup>2</sup> Age of soil on terrace surface

<sup>3</sup> OSL: Optical Stimulated Luminescence, PDI: age derived from soil chronofunction used in Lewis et al (2009)

<sup>4</sup> Strongest, best develop B horizon type in each soil profiles. Subscripts shown are w: color or structure B, k: accumulation of carbonates; t: accumulation of clay; m: cemented

<sup>5</sup> Carbonate stage morphology from Gile et al. (1981) and Birkeland (1999)

<sup>6</sup> PDI values for the 5 Qt3 soils near Albalate are 61.4, 75.1, 64.9, 64.8, 80.8, respectively

Table 3. OSL dates from terraces in the Cinca River valley (adapted from Lewis et al., 2009).

Lab Code	Terrace	Northing	Easting	De (Gy)	Dose rate (mGy/a)	OSL date (ka)
X398	Qt5	4618380	266866	237±26	1.39±0.09	171±22
X399	Qt5	4619473	266357	209±7	1.16±0.7	180±12
X397	Qt6	4618065	266253	157±23	1.62±0.11	97±16
X396	Qt7	4700762	265624	156±26	2.46±0.18	63±12
X1122	Qt7	4700762	265624	128±27	2.16±0.12	59±13
X823	Qt7	4678877	270913	82±15	1.28±0.08	64±13
X197	Qt7	4618846	265647	150±3	2.45±0.12	61±3
X199	Qt7	4613809	267775	101±5	1.80±0.09	56±4
X198	Qt7	4613809	267775	118±5	1.62±0.10	65±5
X817	Qt8	4624970	262087	89.0±10.2	2.26±0.14	39±5
X821	Qt8	4614698	267127	83±10	1.96±0.13	42±6
X833	Qt8	4598786	279236	117±6	2.50±0.16	47±4
X808	Qt8	4598765	278848	88±4	1.75±0.10	50±4
X809	Qt8	4598765	278848	90±2	1.79±0.11	50±3
X828	Qt9	270671	270671	18.3±1.1	1.86±0.12	10±1
X826	Qt9	266149	266149	21.8±0.7	1.89±0.13	12±1
X812	Qt9	266149	266149	18.0±7.6	1.46±0.07	9±4
X813	Qt9	266149	266149	27.0±3.6	1.91±0.10	14±2
X816	Qt9	261783	261783	26.5±1.8	2.15±0.14	12±1
X806	Qt9	263612	263612	23.0±2.3	2.03±0.11	11±1
X807	Qt9	263612	263612	22±1.4	1.96±0.10	11±1
X832	Qt9	275009	275009	18.4±3.6	1.81±0.12	10±2

**Table 4**  
Paleomagnetic data. Location and UTM coordinates (T30), n/N; considered/analyzed samples. Pol: Polarity. Dec/inc: magnetic declination and inclination and the Fisher (1953) statistical parameters (a95 and K).

Terrace	Pit	X (30T)	Y (30T)	Locality	Samples	n	N	Dec	Inc	a95	K	Pol				
Qt7	TA2-1	759,286	4,700,351	Ainsa (Polideportivo)	P85 to P90	3	3	329	32	26.7	33.6	N				
	TA4-1	760,468	4,698,252	Banastón (Caballos)	P77 to P84	2	4	13	38	32.0	125.7	N				
					PCA only	5	7	346	36	24.0	9.0	N				
Qt5	T6-1	766,285	4,619,535	Belver (Plana Valentina)	P01 to P09	6	8	354	64	21.5	12.8	N				
	T6-1	765,701	4,620,590	Belver (Granja Baillarín)	P10 to P15	4	5	350	56	54.3	5.1	N				
Qt4	T7-1	766,023	4,622,346	Belver (Los Almendros)	P16 & P17	2	4	22	49	37.1	94.8	N				
					T7-3	767,682	4,620,960	Belver (Silvio Ballarín)	P44 to P54	3	3	288	55	24.6	10.0	N
									PCA + demagnetization circles	13	13	357	59	12.2	13.6	N
Qt3	T8-1	764,028	4,628,305	Albalate (Los Olivos)	P18 to P24	4	4	26	25	49.7	5.9	N				
	T8-2	763,799	4,627,424	Albalate (El Chopo)	blocks P25 to P28	10	11	5	51	12.0	18.9	N				
	T8-4	764,028	4,628,305	Albalate (Las Lecineras)	P107 to P110	3	3	339	35	31.3	24.9	N				
Qt2	T9-1	765,203	4,629,205	Albalate (Mombrun)	PCA only	14	18	357	47	11.0	13.0	N				
					P55 to P57 + P68 to P70	3	3	153	-71	87.3	4.6	R				
					T9-2	765,126	4,628,812	Albalate (Mombrun)	P103 to P106	4	4	203	-41	5.7	351.1	R
Qt1	T9-3	765,200	4,628,537	Albalate (Mombrun)	P91 to P102	3	3	275	-37	22.9	11.4	R				
					PCA + demagnetization circles	9	10	225	-50	18.0	10.3	R				
Qt1	T10-2	767,495	4,629,475	Albalate (San Salvador)	P29 to P34	6	7	55	74	44.0	2.9	N				
	Cinca Terraces-Reverse					10	10	220	-48	20.6	5.4	R				
	Cinca Terraces-Normal					48	58	355	58	10.6	5.7	N				
	Cinca Terraces-N + R					58	68	8	57	9.8	5.1	N + R				

**Table 5**  
Fluvial incision rates calculated from coupled preserved terraces in the Cinca River valley. Comparison of incision rates at the Ainsa and Albalate sectors is established. Temporal variations of incision rates at the Albalate sector are also evidenced.

Coupled terrace	Differential incision (m)	Elapsed time (Ka)			Incision rate (m/ky)		
		Mean	Minimum	Maximum	Mean	Minimum	Maximum
Qt3-Qt7 Ainsa	128.3	340	219	461	0.38	0.59	0.28
Qt3-Qt7 Albalate	69.6	340	219	461	0.20	0.32	0.15
Qt7-Qt9 Ainsa	38.2	50	45	55	0.76	0.85	0.69
Qt7-Qt9 Albalate	30.3	50	45	55	0.61	0.67	0.55
Qt9-Active channel Ainsa	6.0	11	10	12	0.54	0.6	0.5
Qt9-Active channel Albalate	3.6	11	10	12	0.33	0.36	0.3
Qt1-Qt2 Albalate	49.6	145 <sup>a</sup>	no	no	0.34 <sup>a</sup>	no	no
Qt2-Qt3 Albalate	29.0	488 <sup>a</sup>	no	no	0.06 <sup>a</sup>	no	no
Qt3-Qt5 Albalate	23.6	223	85	361	0.11	0.28	0.07
Qt5-Qt6 Albalate	19.5	81	66	108	0.24	0.29	0.18
Qt6-Qt7 Albalate	26.5	36	26	46	0.74	1.02	0.58
Qt7-Qt8 Albalate	20.8	14	22	6	1.48	0.94	3.45
Qt8-Qt9 Albalate	9.5	36	41	31	0.26	0.23	0.31
Qt9-Active channel Albalate	3.6	11	10	12	0.33	0.36	0.30

<sup>a</sup> Indicative data.

Y (m)	X (m)	Strath elevation (m)	Substrate	Max. rep. grain size (cm)	Location	Distance from headwaters (km)
<b>Qt1 strath</b>						
4626238,7	268814,2	357,31	sst, clay	48	Monte Julia	130,40
4628762,5	268160,6	369,94	clay, sst	48	San Salvador	128,00
4631710,0	266994,0	382,77	clay, sst	43	Brujas	124,70
4633561,1	266598,0	391,65	clay, sst	30	Binaced, pine	123,10
				mean = 42 ± 9		
<b>Qt2 strath</b>						
4622779,0	269090,4	291,86	clay	40	Belver	138,20
4626128,2	267180,0	307,69	sst	42		134,80
4627915,5	266335,7	316,46	clay, sst	48	Mombrun	129,05
4631605,1	265448,4	329,24	clay	36	Binaced 2	125,15
4633506,8	265338,9	333,99	clay, sst	39	Binaced 1	123,35
				mean = 41 ± 4		
<b>Qt3 strath</b>						
4606834,7	275456,5	204,54	clay	34	Zaidin south	155,65
4609076,4	274022,9	212,25	clay	37	Zaidin	153,10
4610459,5	272542,3	221,32	clay	33	San Anton	151,30
4612664,1	272105,5	231,46	ls, clay	33	Zaidin north, peaches	149,45
4615680,8	270893,7	239,25	clay	29	Almudafar	145,45
4617633,2	269497,0	251,03	clay	31	Osso	142,79
4624783,7	265615,0	269,81	clay	32	Albalate, Porquet	132,10
4625718,6	264849,8	278,70	sst	30	Lecineras south	131,25
4627553,2	264705,4	287,57	clay, sst	38	Lecineras north	129,45
4629600,5	264481,2	299,33	clay	33	Las Brujas west	126,85
4630292,1	264604,0	300,16	clay	33	Las Brujas west	126,60
4631856,3	263793,9	302,45	clay	46	Alfantega-Albalate	125,15
4633829,1	264075,3	312,84	sl, sst	33	Alfantega south	123,05
4635456,3	264683,0	324,76	sst, clay	41	Alfantega north	121,60
4641433,4	267164,4	348,76	sst	33	Monzon south	114,30
4642139,0	267230,3	351,28	clay	31	Monzon, cemetery	113,60
4643345,2	267354,5	359,67	clay	NA	Monzon, castle	112,80
4648994,7	264935,1	384,64	sst clay	35	Castejon, gravel pit	108,20
4650942,7	264077,2	382,30	gyp	NA	Castejon-Salinas	106,10
4651648,2	264273,7	398,07	gyp	NA	Castejon	104,70
4652887,4	269341,9	393,82	clay	26	Fonz 3	104,55

4656953,7	265155,5	427,86	sst, clay	26	Las Coronas 3	100,05
4657059,2	265420,3	424,30	clay, sst	34	Las Coronas 1	99,95
4657890,1	265794,1	427,42	clay, sst	35	Las Coronas 4	98,95
4659224,5	266451,3	435,14	cgl, sst	NA	Las Coronas 2	97,80
4673397,6	270716,4	507,73	cgl	NA	Torreciudad 2	81,55
4673470,8	270762,6	511,44	cgl, clay	NA	Torreciudad	81,55
4674106,1	270586,2	519,12	clay	NA	Torreciudad north	80,90
4679386,0	270652,0	533,57	clay	35	Abizanda-Moscarazos	75,70
4698766,8	267451,0	687,52	sst, marls	50	Santa Tecla	55,80
4698820,7	267324,8	685,63	marls	NA	Santa Tecla	55,80
4699527,8	267293,3	698,75	marls, sst	NA	Arnal	54,55

mean = 34 ± 6

**Qt4 strath**

4618310,2	268999,2	234,51	clay	41	Osso	142,00
4621360,8	267202,7	249,02	clay	27	Belver	138,50
4623856,0	265718,1	264,08	clay	31	Albalate	134,65
4632761,8	263831,0	299,94	clay, sst	41	Alfaltega south	124,20
4633014,6	263912,7	301,32	cl	43	Binaced road	123,95
4647516,3	264286,8	356,10	clay, sst	26	Castejon, horse arena	109,85
4648272,3	264594,9	360,26	sst, clay, gyp	NA	Castejon 1	109,05
4648923,5	265099,9	363,73	sst	NA	Castejon, gravel pit	108,20
4654312,1	269983,2	397,45	clay	NA	Fonz 1	100,95
4657383,2	270205,3	410,16	clays	NA	Fonz 2	97,95
4671239,3	271297,4	478,68	cgl, sst, clays	NA	El Grado	83,90

mean = 35 ± 8

**Qt5 strath**

4604667,1	276619,5	175,11	clay, sst, lm	28	Pilaret-Fraga 1	158,35
4606841,1	275133,3	185,07	clay, marls	36	Zaidin south	155,45
4608012,4	273923,2	189,64	clay	NA	Zaidin	153,85
4612314,6	270700,4	202,56	clay, sst	39	Zaidin	148,70
4615106,6	269791,6	219,61	clay	51	Almudafar	146,00
4617641,2	268022,3	226,21	clay	29	Osso	142,10
4620596,2	266439,1	235,60	clay	38	Belver	138,70
4623348,5	264910,9	254,56	clay, sst	46	Albalate	134,90
4625398,1	264561,8	257,27	clay	NA	Lecineras	131,50
4627116,2	264081,3	268,53	clay	37	Clamor	129,90
4629659,3	263752,5	279,92	clay	37	Alfantega-Albalate 2	126,75
4631764,0	263530,5	285,61	sst, clay	41	Alfantega-Albalate 1	125,30

mean = 38 ± 7

**Qt6 strath**

4612095,2	270574,9	184,55	clay	31	Zaidin	148,80
4614561,5	268279,5	192,57	clay	24	Almudafar	145,40
4617395,8	266899,7	205,17	clay	38	Osso	141,75
4619988,9	265939,2	215,59	clay, sst	46	Belver	139,00
4662716,8	271705,9	362,57	sst, marls	30	Estada	98,45
4668560,4	272171,0	416,16	sst	27	Artasona	86,45
4710107,9	264958,2	673,64	not seen	80	Laspuna	43,05
4710475,2	265867,2	683,96	marls	NA	Laspuna	42,90

mean = 39 ± 19

**Qt7 strath**

4603962,4	276944,5	136,17	clay, silt	20	Pilaret	159,15
4608542,3	272710,3	148,99	ls	23	Zaidin south	152,80
4609939,6	271780,7	154,18	ls, clays	25	Zaidin	151,00
4611129,6	270605,8	165,74	clay, ls	22	Ave	149,60
4612328,1	269279,9	167,12	clay	22	Almudafar south	147,55
4613510,6	268000,6	171,28	clay	30	Almudafar south 2	145,95
4613818,8	267774,6	170,83	sst?	24	Almudafar, gravel pit	145,55
4614506,9	267304,1	172,25	sst, clay	31	Almudafar north	144,65
4615711,5	266825,8	177,04	ls, clay	25	Osso south	143,60
4617975,1	266027,5	188,40	cl?	22	Osso north	140,75
4618821,2	265551,1	190,81	sst, ls, clay	29	Belver, Tejerias	139,75
4619145,8	265392,6	189,07	clay	31	Belver	139,65
4621596,7	264063,9	199,87	sst, silt	28	Albalate	136,35
4621619,2	264052,5	199,71	sst, silt	NA	Albalate	136,35
4622728,3	263753,3	204,00	silt, sst	29	Albalate	135,20
4623531,0	263013,5	207,42	clay, sst	29	Albalate	134,20
4623528,9	259973,4	203,89	silt, clay	31	Alcolea	133,25
4625094,6	259311,4	209,43	clay	27	Alcolea north	132,74
4624817,7	262567,7	208,95	clay	35	Albalate km 1	132,30
4625514,2	259383,6	209,85	clay	NA	Alcolea north 2	131,65
4626568,0	259527,9	213,21	clay?	25	Santa Lecina, Viruelas	130,70
4626521,5	262161,2	216,06	clay, sst	25	Albalate km 3	130,45
4629220,0	260490,3	222,01	sst	25	Santa Lecina south	129,60
4628634,8	262493,1	228,18	sst, clay	NA	Albalate km 5.5	128,60
4628801,0	262431,0	226,97	clay	NA	Albalate km 6	128,30
4628801,1	262430,8	227,67	clay	35	Albalate km 6	128,30
4630222,5	260538,4	228,20	clay	31	Santa Lecina north	126,60
4631295,0	262957,6	235,87	sst, clay	47	Albalate km 8	125,85

4631388,9	263081,3	237,28	sst	37	Albalate km 8	125,85
4631924,0	260920,1	234,55	st, clay	NA	Estiche south	125,45
4633048,6	263181,9	241,37	clays	37	Binaced road	123,95
4633660,7	260901,2	242,52	clay, sst	39	Estiche	123,80
4634429,6	263302,9	246,29	clay	37	Alfantega south	122,77
4635076,2	263518,3	248,91	clay	28	Alfantega	122,45
4635076,0	263519,1	248,84	clay	NA	Alfantega	122,05
4635999,8	261450,7	250,32	clay, sst	23	Estiche north	121,50
4637344,9	263780,0	258,93	sst, clay	34	Pueyo	119,85
4637984,2	261620,5	261,21	clay	22	Pomar north	119,50
4639441,3	264658,1	269,06	sst, clay	NA	Pueyo	117,80
4639697,2	262563,3	265,73	clay, sst	NA	Conchel south 2	117,80
4639713,5	262565,1	276,29	clay, sst	26	Conchel south 2	117,80
4640762,0	263112,8	269,41	sst, clay	27	Conchel	116,65
4640326,8	264903,1	270,19	clay, sst	32	Alegria	116,55
4641521,3	263719,4	274,05	sst	28	Conchel north	115,65
4643649,4	264741,5	283,85	sst	31	Selgua	113,35
4645806,7	265061,4	292,63	clay, sst	29	Monzon north	111,25
4647577,6	265271,7	295,37	sst, clay	NA	Castejon, concrete plant	109,55
4647937,3	265274,5	302,00	sst	NA	Castejon (repeat)	109,05
4647937,5	265275,1	302,98	sst, clay	40	Castejon	109,05
4648783,4	266670,7	310,82	not seen	NA	Chula Vista	107,95
4648737,8	266624,3	309,66	sst, clay	NA	Chula Vista	107,95
4648783,4	266670,7	310,82	sst, clay	30	Chula Vista	107,95
4649518,1	267381,8	307,92	gyp	29	Ariestolas	107,45
4653028,9	268364,0	324,47	clay?	27	Cofita	104,15
4655141,4	267896,4	338,23	sst	39	Fonz	100,80
4657703,6	267937,3	341,73	sst, cgl, clay	34	Arias II	98,40
4658881,1	268853,8	344,51	cgl	41	Casa Pararayos	96,50
4659779,8	269184,5	349,60	sst	40	Central Electrica Pilas	95,70
4662686,0	269983,7	364,44	clay, sst	41	Enate	93,10
4664323,9	270860,5	372,14	clay, sst	48	Enate north	90,90
4665668,4	271111,9	383,23	cgl, sst	33	El Grado south	89,45
4666272,9	271795,1	378,93	sst, cgl	32	Olvena	88,90
4667415,4	271756,1	385,12	sst, cgl	35	Artasona south	87,60
4669740,5	270777,3	400,65	clay	42	El Grado	85,35
4670069,9	271665,4	408,35	sst	51	El Grado dam 2	85,05
4670299,3	271420,3	402,16	ls	44	Dam	84,75
4678793,0	270908,2	449,57	marls?	55	Moscarazos	76,05
4684220,2	270139,2	479,93	ls, marls	33	Liguierre	70,50

4685135,5	270156,0	488,43	Triassic red beds	53	Liguerre2	69,60
4692888,6	268198,3	525,39	marls	NA	Ainsa, airport	61,40
4696062,9	267620,1	543,96	marls	30	Gerbe	58,45
4697188,3	266541,9	550,44	sst, marls	42	Banaston	57,00
4698268,3	266398,0	559,25	marls	NA	Banaston 2	55,85
4699552,2	266071,0	566,39	sst	NA	Usana	54,55
4700761,5	265623,9	568,12	marls	NA	Pueyo-Ainsa	53,30
4703367,9	265076,6	587,06	marls	NA	Ainsa north	50,40
4703968,8	264325,4	599,71	marls	NA	Labuerda	49,80
4709582,2	265366,6	650,20	marls	NA	Escalona	43,60
4709906,5	265387,2	653,19	marls	NA	Escalona2	43,25
4709912,6	265032,2	655,82	marls	NA	Escuain hwy	43,20
4710744,3	265700,3	662,57	marls	40	Laspuna	42,55
4711889,9	265799,1	664,36	marls	NA	Laspuna north	41,45
4714062,0	266742,2	697,85	ls	NA	Misuellas	38,90
4713888,6	269696,5	718,61	marls	68	Badiain	35,40

33 ±9

**Qt8 strath**

4590370,1	279052,3	80,17	ls	NA	Escarpe, convent	172,40
4590370,5	279052,6	80,24	ls	NA	Escarpe, convent	172,40
4590891,4	279123,9	80,10	ls	25	Masalcorreig	171,80
4590945,9	279117,4	81,53	ls	NA	Masalcorreig	171,80
4591745,5	279254,7	86,95	ls	NA	Masalcorreig	171,05
4592329,1	279302,0	85,93	marls, ls	23	Masalcorreig south	170,35
4593975,4	279633,5	91,86	sst, clay	27	Masalcorreig north	168,85
4597707,6	279414,7	105,00	clay,sst	NA	Fraga south	166,65
4598786,9	279212,5	108,89	clay,sst	NA	Fraga hwy work	163,95
4599957,9	278910,1	111,15	sst, clay	NA	Fraga	162,90
4606658,0	274037,9	125,52	clay, sst, ls	NA	Clamor, confluence	154,85
4607369,5	271680,2	137,35	clay	28	Velilla	152,90
4610224,5	268472,5	158,00	clay	25	Velilla, Ave	148,55
4612890,9	267490,8	145,63	clay	31	Almudafar south	146,15
4615161,1	266942,4	158,30	clay, sst	25	Almudafar north	144,05
4614753,1	265034,6	157,11	clay, marls	25	Chalamera-Ballobar	143,10
4616088,7	266511,0	166,68	clay	NA	Osso	142,65
4617565,5	265856,2	162,10	clay	35	Osso north	141,15
4617332,9	263643,4	180,52	clay	42	Chalamera	140,15
4618685,0	262929,1	179,86	clay	36	Chalamera, hermitage	138,75
4624667,5	262009,9	188,57	?	22	Albalate	133,90
4651338,4	267816,2	299,06	gyp	28	Cofita south	105,65

4652421,1	267841,3	305,88	gyp, marls	27	Cofita, canal	104,65
4660668,2	269984,0	336,43	Keuper facies	NA	Estadilla	94,50

mean = 29 ± 6

**Qt9 strath**

4596667,0	279164,7	93,79	clay, sst	12	Fraga toll rd	160,45
4603299,3	275311,1	101,25	sst, clay	28	Miralsot south	152,75
4605605,7	275012,0	116,38	sst, clay	31	Zaidin south, gravel pit	150,60
4615652,4	265127,9	152,28	clay?	22	Chalamera-Ballobar	136,95
4618197,2	263357,3	159,90	sst, clay	28	Chalamera, hermitage	133,70
4620341,8	264057,6	168,05	clay	24	Albalate-Belver	131,85
4623545,6	262027,5	177,68	?	15	Albalate	128,25
4626222,8	261433,0	184,79	sst	34	Las Torres	125,50
4627246,1	261894,9	190,18	sst	26	Ciguena	124,50
4632191,0	262278,6	205,64	sst	12	Soto del Tros north	119,40
4633967,1	262899,7	213,73	clay, sst	60	Alfantega	117,55
4636516,8	262991,4	220,84	cl	26	Pueyo	115,25
4641308,4	264711,2	241,67	sst	21	Alegria	110,00
4642910,2	265578,5	244,41	sst	NA	Monzon south	108,40
4644355,7	266152,6	251,55	sst, clay	22	Sosa confluence	106,70
4646366,6	265770,4	263,05	sst	21	Monzon north	105,05
4648800,4	266119,5	267,70	sst	NA	Castejon 2	102,45
4648906,0	266183,6	271,11	sst	NA	Castejon 1	102,45
4665046,2	272113,9	341,86	not seen	21	Esera confluence	84,35
4667582,6	270679,9	358,33	not seen	NA	El Grado south	81,70
4669267,9	270600,1	369,16	not seen	37	El Grado south	80,40
4686475,7	270644,5	446,97	ls	NA	Liguerre, bridge	62,95
4698725,7	265976,7	524,26	marls (approx.)	48	Usana	49,60
4710107,5	265784,0	612,75	marls	40	Laspuna	37,50
4711924,7	265460,0	627,23	marls	45	Laspuna	35,90
4714416,3	266839,4	657,03	marls	38	Hospital de Tella	32,75
4714170,9	269863,3	692,99	ls, marls	NA	Lafortunada	29,90

mean = 29 ± 12

**Active channel**

4590568,2	278243,3	76,16		NA	Torrente south	167,50
4592675,2	279204,4	74,58		NA	Masalcorreig	166,50
4594870,8	278388,8	79,66		NA	Torrente de Cinca	164,60
4596928,2	278849,5	86,71		NA	Fraga toll rd	162,50
4598806,7	278948,2	91,45		NA	Fraga	160,20
						158,35

4598821,9	278940,5	87,89		NA	Fraga circunvalacion	158,35
4600248,2	278725,2	94,51		NA	Fraga	157,25
4601693,1	278159,6	98,36		NA	Zaidin-Fraga 4	155,95
4603247,8	277358,1	101,14		NA	Zaidin-Fraga 3	154,25
4604209,4	276322,3	106,41		NA	Miralsot south	152,70
4605611,4	274968,5	105,92		NA	Zaidin south, gravel pit 2	150,75
4606472,3	274068,0	112,86	ls	NA	Zaidin-Fraga 2	149,55
4608479,0	272650,7	119,77		NA	Zaidin 1	147,05
4609465,8	271366,8	120,59	ls	NA	Zaidin	145,70
4610187,2	269704,0	129,27		NA	Ave south	144,05
4610378,3	268514,1	128,03		NA	Ballobar, Ave	143,00
4612062,3	267550,6	133,60		NA	Almudafar south	141,15
4613488,6	266644,3	140,72		NA	Almudafar	139,45
4615639,9	265193,2	147,30		NA	Chalamera-Ballobar	137,00
4616710,9	264612,4	148,82		NA	Chalamera	135,55
4618298,0	263415,2	155,20		NA	Chalamera, hermitage	133,20
4618566,0	263392,3	160,45		NA	Belver	133,40
4619667,1	263075,0	166,23		NA	Belver north	132,30
4620039,9	262992,4	159,69		NA	Albalate south	132,22
4622262,0	262463,6	169,12		NA	Albalate south	129,75
4623423,1	261865,3	176,13		NA	Albalate	128,30
4623430,2	261865,1	175,24		NA	Albalate	128,35
4626195,7	261399,3	180,14	sst	NA	Las Torres	125,50
4627618,6	261822,7	185,31	sst	NA	Ciguena	123,95
4630745,8	261361,0	196,13		NA	Soto del Tros	120,95
4633356,8	261767,0	207,86		NA	Estiche	118,35
4637273,7	262133,7	221,03		NA	Pomar	114,80
4639503,1	262665,8	228,24		NA	Pueyo	112,35
4640927,9	263980,0	235,68		NA	Conchel	110,60
4643437,3	265673,5	241,04		NA	Selgua-Monzon	107,60
4644809,6	265867,9	250,61		NA	Monzon	106,35
4646194,6	265594,6	257,47		NA	Monzon north	105,15
4648060,5	265631,7	258,81		NA	Castejon	103,40
4648969,3	266539,5	263,55		NA	Castejon 2	102,20
4650585,0	265670,5	273,82		NA	Castejon 3	101,05
4652004,2	265839,1	277,07		NA	Cofita	99,10
4653915,1	265547,3	285,08		NA	Vero confluence	97,20
4655130,7	266128,3	288,41		NA	Vero confluence north	96,00
4658190,6	266885,9	299,79	sst, cgl dipping 45N	NA	Arias II	92,85
4659504,4	267534,9	306,99		NA	Coronas north	91,50

4660935,1	269750,3	319,45	NA	Puente las Pilas	88,90
4662402,9	270235,1	329,67	NA	Enate 2	87,35
4663979,8	271147,6	336,60	NA	Enate	85,60
4665299,6	271386,7	346,06	NA	Piscifactoria	84,10
4666952,5	271084,7	349,10	NA	Artasona south	82,65
4669068,8	271402,9	358,94	NA	El Grado	80,50
4670028,2	271513,5	365,31	NA	El Grado dam	79,50
4672400,0	271300,0	380	NA		77,15
4677400,0	271000,0	400	NA		72,10
4681300,0	272500,0	420	NA		68,10
4686300,0	274000,0	440	NA		63,05
4889100,0	270000,0	460	NA		60,15
4692750,0	268750,0	480	NA		56,30
4696800,0	266450,0	500	NA		51,55
4699976,5	264920,2	528,59	NA	Ainsa	48,25
4702081,1	264805,0	541,17	NA	Ainsa north	46,05
4704007,1	264807,9	555,85	NA	Labuerda	44,15
4706553,1	265675,7	575,91	NA	Labuerda north	41,35
4710050,0	265753,7	601,17	NA	Laspuna, bridge	37,50
4711829,8	265405,3	617,64	NA	Laspuna north	36,00
4711989,0	265561,9	623,30	NA	Puertolas	35,60
4712750,6	266107,4	633,25	NA	Puertolas north	34,80
4713987,4	266833,0	644,17	NA	Misuellas	33,15
4714366,8	268440,4	661,44	NA	Laspuna reservoir	31,40
4715470,8	270601,9	697,83	NA	Devotas	28,05
		740	NA		25,70
4718416,4	270829,7	753,47	NA	Salinas	25,05
		780	NA		23,70
		800	NA		23,45
4720183,9	273539,0	900,84	NA	Bielsa south, gorge	21,70
4723000,2	272895,7	973,66	NA	Bielsa	18,65
4724306,0	271381,9	1087,65	NA	Javierre	16,45
4725075,8	268267,4	1161,20	NA	Pineta 2	12,95
4729158,6	261407,7	1273,24	NA	Pineta	5,25
		1300	NA		4,25
		1400	NA		3,75
		1500	NA		3,35
		1600	NA		2,95
		1700	NA		2,75
		2100	NA		2,25

2200	NA	2,10
2500	NA	1,25
2520	NA	0,75
2600	NA	0,25
2700	NA	0,03